

# State-of-the-Art Review of Design of Experiments for Physics-Informed Deep Learning

Sourav Das<sup>1\*</sup> and Solomon Tesfamariam<sup>1</sup>

<sup>1\*</sup>School of Engineering, The University of British Columbia, Okanagan Campus, 3333  
University Way, Kelowna, V1V1V7, BC, Canada.

\*Corresponding author(s). E-mail(s): [sds2019@mail.ubc.ca](mailto:sds2019@mail.ubc.ca);  
Contributing authors: [solomon.tesfamariam@ubc.ca](mailto:solomon.tesfamariam@ubc.ca);

## Abstract

This paper presents a comprehensive review of the design of experiments used in the surrogate models. In particular, this study demonstrates the necessity of the design of experiment schemes for the Physics-Informed Neural Network (PINN), which belongs to the supervised learning class. Many complex partial differential equations (PDEs) do not have any analytical solution; only numerical methods are used to solve the equations, which is computationally expensive. In recent decades, PINN has gained popularity as a replacement for numerical methods to reduce the computational budget. PINN uses physical information in the form of differential equations to enhance the performance of the neural networks. Though it works efficiently, the choice of the design of experiment scheme is important as the accuracy of the predicted responses using PINN depends on the training data. In this study, five different PDEs are used for numerical purposes, i.e., viscous Burger's equation, Schrödinger equation, heat equation, Allen-Cahn equation, and Korteweg-de Vries equation. A comparative study is performed to establish the necessity of the selection of a DoE scheme. It is seen that the Hammersley sampling-based PINN performs better than other DoE sample strategies.

**Keywords:** Design of Experiment, Deep Learning, Physics Informed Neural Network, Uncertainty Quantification

## 1 Introduction

Quantifying uncertainties in a physical system is an active area of research in the science and engineering fields [1]. In design optimization under uncertainty, Monte Carlo simulation (MCS) [2] is the oldest and most widely used technique. The MCS, however, requires large number of model evaluations and computationally is costly for high-fidelity models. Surrogate-assisted models, developed using Design of Experiment (DoE) (Fig. 1), are attractive options.

Once the training data-set through the DoE are generated, different methodologies are used to build the surrogate model (Fig. 1), e.g. response surface method [3], stochastic response surface method [4], polynomial chaos expansion (PCE) [5, 6], Kriging [7, 8], PCE-Kriging [9], high dimensional model representation (HDMR) [10, 11], radial basis function (RBF) [12, 13], support vector regression (SVR) [14], artificial neural network [15], ensemble surrogate [16], etc. The surrogate models minimize the noise between actual and predicted responses using fitting tools (shown in Fig. 1), based on the knowledge of DoE samples.

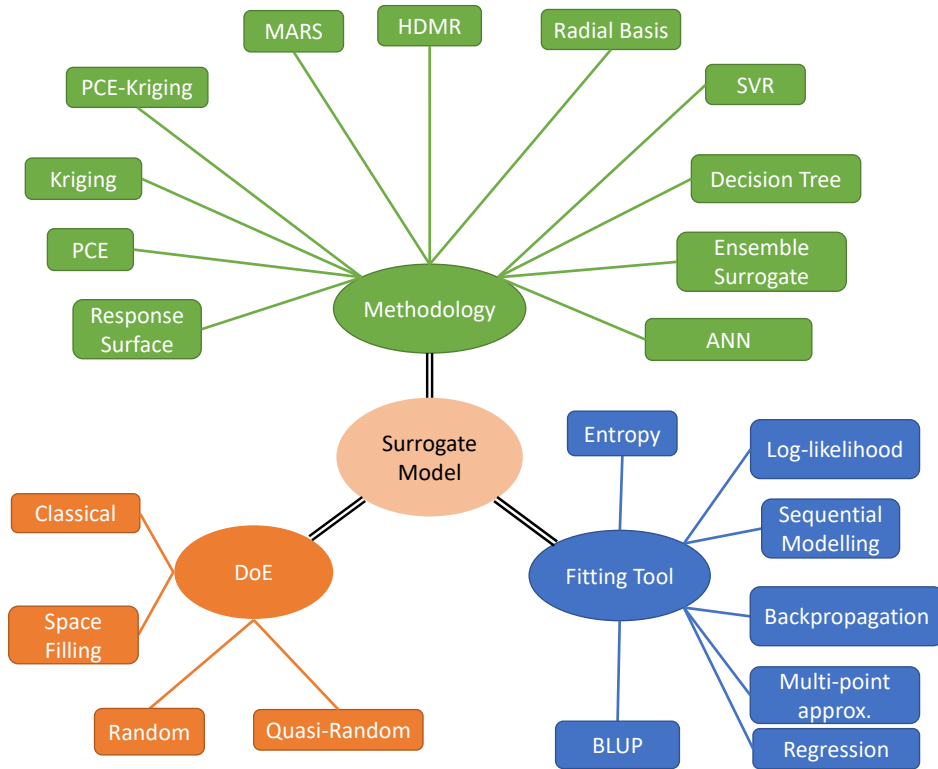


**Fig. 1** A schematic diagram shows the commonly used surrogate models

The purpose of using DoE is that the samples should cover the entire design space; otherwise, predicted responses will be erroneous. Fig. 1 illustrates a schematic diagram of the commonly used surrogate models, DoE schemes and the fitting tools.

Machine learning is a widely used methodology to develop forecasting models and support decision making under uncertainty [17, 18]. The recent research trends devote on the machine learning techniques that can be used as a surrogate model for regression analysis. Feed-forward neural networks, which is a special class of supervised machine learning technique, a data-driven network, is used in this paper. In this study, we are focusing only on physics-informed neural networks (PINNs), where physical conditions are imposed on feed-forward neural network. The PINN has been widely used in various fields. An overview of variants and applications of PINN is presented here. Raissi and Karniadakis [19]

proposed PINN to identify parameters in partial differential equations (PDEs) like the Kortewegde Vries Equation and the Navier-Stokes Equation [20]. The solution to the alloy solidification benchmark problem was investigated by Rad *et al.* [21]. Shin *et al.* [22] showed the convergence of PINN to solve PDEs towards the theoretical solution of PDEs using the Schrader approach. PINN is also used to solve physical problems by replacing the finite element method (FEM). Haghghat *et al.* [23] used PINN to solve the linear elastic problems in the field of solid mechanics. The direct and inverse heat conduction problems of materials were studied by He *et al.* [24]. Olivieri *et al.* [25] proposed a PINN based methodology for near-field acoustic holography for contact-less analysis of vibrating structures. PINN is also used to forecast the remaining useful life (RUL) of the rotating machinery in wind farms. Eker *et al.* [26] proposed a physics-informed model for short-term

prediction of the RUL of the rotating machinery. Yucesan and Viana [27] studied wind turbine main bearing fatigue using PINN. Its application is extended into fluid-structure interaction problems. The performance of vortex and wake induced vibration of the cylinder is studied by Cheng *et al.* [28] using PINN based on Reynolds Average Navier Stokes equations. Bai and Zhang [29] extended the above work from laminar flow to turbulent flow by adding viscosity into the equations using PINN. To forecast the flow field without any simulation, Sun *et al.* [30] proposed a PINN-based framework which includes the physical equations, initial and boundary conditions. Tang *et al.* [31] proposed a transfer learning based PINN to enhance learning efficiency for vortex induced vibration. Another application of the civil engineering field is seismic wave propagation, where time domain wave equations are computationally expensive as they need a lot of memory to store the wavefield solutions. With this in view, Song *et al.* [32] proposed a PINN-based framework to solve the Helmholtz equation for obtaining wavefield solutions. Karimpouli and Tahmasebi [33], Alkhalifah *et al.* [34] demonstrated the efficacy of PINN in modelling the wave equation in the time- and frequency-domain. The solutions of isotropic and anisotropic  $P$ -wave eikonal equations using PINN were shown by Smith *et al.* [35], Waheed *et al.* [36]. To solve the scattered pressure wavefield, Alkhalifah *et al.* [34] proposed a PINN-based framework. The other applications of PINN are discussed briefly. Patel *et al.* [37] investigated thermodynamically consistent PINN for hyperbolic shock hydrodynamics systems. The forward and inverse problems related to the nonlinear diffusivity and Biot's equation were investigated by Kadeethum *et al.* [38]. They also studied the effects of noisy measurements on inverse problems and addressed the challenge of selecting the hyperparameters of the inverse model. Lu *et al.* [39] proposed a deep learning algorithm for topology optimization that includes PINN and hard constraints. Schiassi *et al.* [40] proposed a novel technique of PINN for the solution of point kinetics equations with temperature feedback for nuclear reactor dynamics. They developed a framework that is a combination of PINN with the Theory of Functional Connections and Extreme Learning Machines. The corrosion fatigue modeling, consisting of crack growth and damage bias due to

corrosion of the aircraft wings, was proposed by Dourado and Viana [41] using PINN. The multifidelity simulation technique, which is a combination of low-fidelity and high-fidelity simulations using PINN, was studied by Penwarden *et al.* [42] to reduce the computational cost. Kovacs *et al.* [43] used PINN to solve magnetostatic and micromagnetic problems. The design of electromagnetic metamaterials using PINN was proposed by Fang and Zhan [44]. Aside from the applications of PINN in various fields, various variants of PINN have been developed, such as conditional PINN [45], conservative PINN (cPINN) [46], variational PINN (vPINN) [47], parareal PINN (pPINN) [48], stochastic PINN (sPINN) [49], fractional PINN (fPINN) [50], nonlocal PINN (nPINN) [51], extended PINN (xPINN) [52] etc. Shukla *et al.* [53] proposed a domain decomposition based parallel PINN where all hyperparameters of each neural network are optimized separately in each sub-domain. Kharazmi *et al.* [54] proposed a novel  $hp$ -Variational PINN based on the sub-domain Petrov–Galerkin method where domain decomposition was used as  $h$ -refinement and projection onto space of high order polynomials was used as  $p$ -refinement.

The outline of the article is structured as follows. Section 2 describes an overview of DoE schemes. Section 3 provides a comprehensive summary of machine learning techniques in general and PINN. Different applications of PINN using the DoE schemes are presented in Section 4. Finally, Section 5 presents the concluding remarks.

## 2 Design of Experiment Sampling Strategy

Experiments used to be performed by trial-and-error to find sample (or training samples or support) points [3]. Fisher [55] introduced the concept of a design of experiment (DoE) strategy in the early 20th century for investigating the probabilistic behaviour of agricultural crop systems. The DoEs are used in the engineering field [56, 57] and are gaining popularity due to the reduction in computational costs. The DoE can be grouped into two categories, i.e., Classical DoE [3, 58–61] and Modern DoE [57, 62–64]. The DoE samples are generated using two approaches, i.e., domain-based (or non-adaptive or model-free)

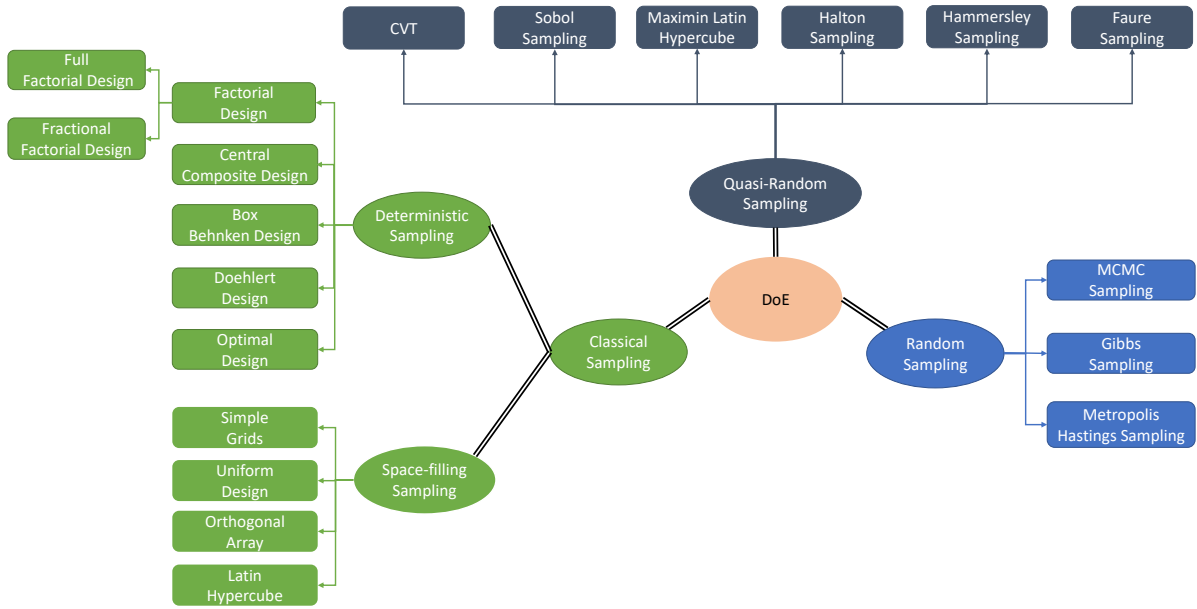


**Fig. 2** Commonly used DoE sampling strategies

and response-based (or adaptive or model-based or sequential) approaches. In the domain-based approach, the DoE samples are generated based on the information obtained from the design space, whereas in the response-based approach, the samples are chosen from the information obtained from the surrogate models. In this paper, extensive reviews on generation of DoE sample strategy are presented. The study is mainly focused on four different sampling schemes, i.e., deterministic sampling (classical DoE), space-filling sampling, random sampling, and quasi-random sampling. The DoE schemes are shown in Fig. 2 and further discussed below.

In the deterministic scheme, the sample points are generated uniformly over the design space, and the number of sample points is also fixed with the aim of minimizing the random error of the simulation. Therefore, the samples are generated in such a manner that most of the samples are located at the boundary of the design space, with few samples in the interior space. There are various type of classical DoE scheme available, factorial design [3], central composite design [65], Box-Behnken design [66], optimal design [67], etc. Space-filling sampling also lies within the classical DoE approach. This sampling technique is mainly used to enhance accuracy of the surrogate models. Initially, a surrogate model is built with few samples, and that

model is updated iteratively by adding a sample to the previous DoE set used until a satisfactory accuracy is achieved. In this category, simple grids, Latin hypercube [68], orthogonal array [69], and uniform design [70] are the most popular DoE generation schemes.

Random sampling and quasi-random sampling lie within the modern DoE approach. In random sampling, Markov chain Monte Carlo (MCMC) sampling, [71], Gibbs sampling [72], and Metropolis-Hastings sampling [73] are popular. The samples are generated with an equally likely probability of occurrence of samples within the design space. This technique is suitable only when the proper knowledge of design space is available because the clustering or poor coverage regions of samples have been observed for high-dimensional problems. In quasi-random sampling, the popular schemes are centroidal Voronoi tessellation (CVT) [74], maximin Latin hypercube [75], Sobol sampling [76], Halton sampling [77], Hammersley sampling [78], Faure sampling [79], etc.

## 2.1 Full & Fractional Factorial Design

Factorial design is one of the oldest techniques for the design of experiment samples [3]. Every

input variable is discretized into two or three levels. Fig. 3(a) shows a two-level full factorial design. Every input variable is bounded by lower and upper limits, which are the minimum and maximum values of the variable, expressed by (-1) and (+1). For three-level factorial design, a sample point is taken at the center of the variable, which is the mean value of the input variable. More concisely, a two-level design takes sample points at the lower and upper limits of the variable, whereas a three-level design takes sample points at the lower, upper, and center. In general, the number of runs or simulations required is expressed as  $2^n$  or  $3^n$  for two- and three-level designs, respectively, where  $n$  is the number of input variables. Fig. 3(a) shows a  $2^3$  full factorial design.

Though full factorial design is easy to use, it has some drawbacks as the number of runs or simulations depends on the number of input variables considered. For high dimensional problems, the number of runs increases with an increasing number of variables, which becomes computationally expensive for high-fidelity models. The fractional factorial design lowers the computational cost where fewer sampling points are generated than in the full factorial design. For fractional factorial design, the number of samples is expressed as  $2^{n-k}$  and  $3^{n-k}$ , for two- and three-level design, respectively. Fig. 3 depicts a  $2^3$  design, i.e. two-level and three factors for full and fractional factorial design. Though factorial design is a commonly used DoE scheme, it fails to capture the nonlinearity of the system responses as it considers only the lower, center, and upper values of the variables.

## 2.2 Central Composite Design

The central composite design (CCD), proposed by Box and Wilson [65], is a variant of factorial design where additional sampling points are considered at the center and axial directions. Fig. 4 shows the two-level CCD for three factors. The extremity samples are located at the lower and upper limits of each variable, which is the same as in full factorial design. Additionally, two axial points for each variable and the center point of the hypercube are considered. For a two-level central composite design, the number of simulations required for a given number of input variables is  $2n + 2n + 1$ . The CCD are categorized into three types, i.e., circumscribed (CCC), inscribed (CCI) and faced

(CCF). In the CCC design, the axial points are located at the outside of the cube where the cube points take (-1) and (+1) values. CCI design is the same as CCC design, but scaled where the axial points are taken (-1) and (+1) values and cube points are located inside the cube. Unlike in CCC design, where axial points are located on the outside of the cube, in CCF design, the axial points are placed on the face of the cube. Fig. 4 shows all three types of CCD for three factors.

## 2.3 Box-Behnken Design

The Box-Behnken design (BBD) [66] is similar to CCD, where the sample points are located at the midpoint of each edge and one at the center of the hypercube. It does not have any corners or extreme points. Fig. 5 illustrates the Box-Behnken design for three factors. A comparison of DoE samples obtained from all types of CCD and BBD is shown in Table 1 for three factors. It is seen that BBD requires less number of simulations compared to other CCDs. Like factorial design and CCD, it also suffers “curse of dimensionality” for high dimensional problems as the number of simulations increases with the increasing number of input variables, which affect the computational cost.

## 2.4 Doehlert Design

Doehlert [80] proposed another efficient design of experiment scheme that takes fewer simulations than CCD and BBD. This strategy has been proven more economical and highly-efficient than other deterministic DoE sample strategies [81]. The main difference between this design and CCD and BBD is that the samples generated from the Doehlert design are not rotatable due to the number of estimations for different input variables or factors. At the same time, this design is efficient in filling the space uniformly. Doehlert design provides different structure for the different number of factors such as, for two variables, samples are generated by forming a circular domain. For three factors, it becomes spherical domain and for four or more factors, it becomes hyperspherical domain [82]. This design allows the total number of simulation as  $n^2 + n + 1$ , where  $n$  is the number of simulation factors. Fig. 6 illustrates the Doehlert design for two and three factors. Table 1 shows the comparison of number of samples generated

## State-of-the-Art Review of Design of Experiments for PINN

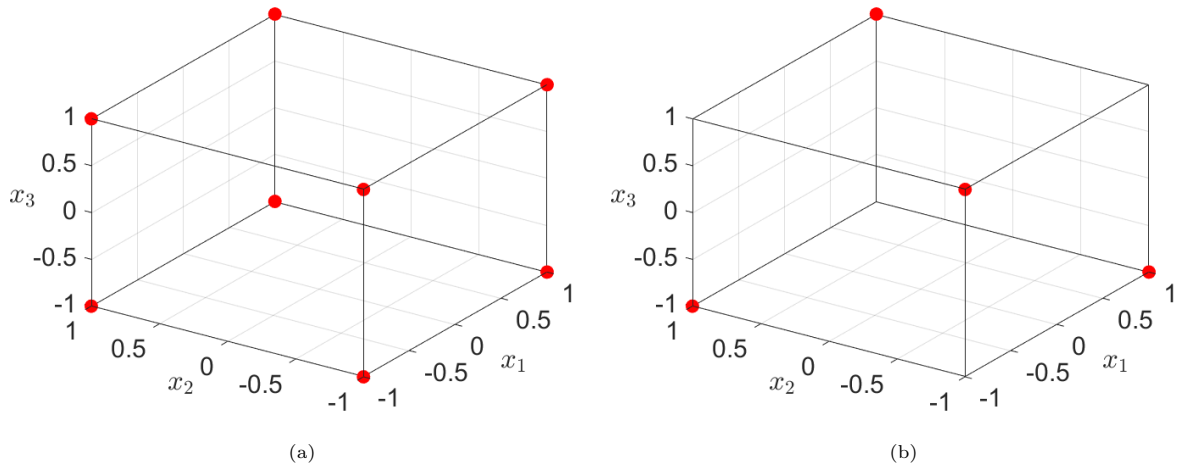


**Fig. 3** 2-levels (a) full and (b) fractional factorial design

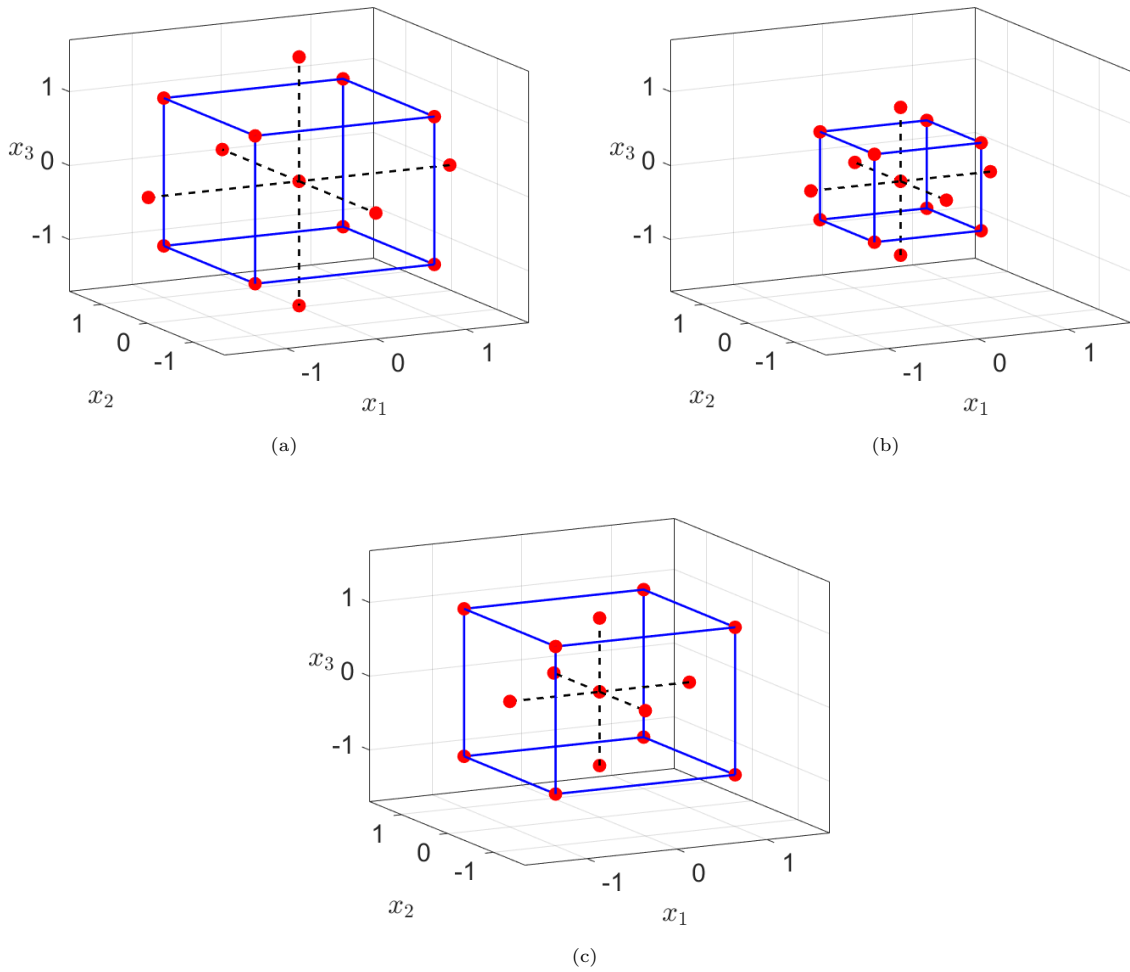


**Fig. 4** Central composite design; (a) Circumscribed, (b) Inscribed and (c) Faced

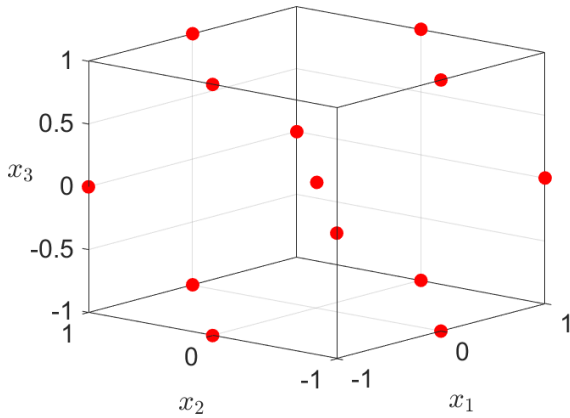


**Fig. 5** Box-Behnken design

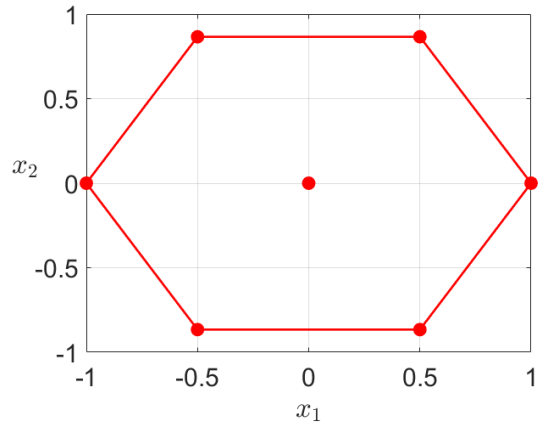
using factorial, central composite, Box-Behnken and Doehlert design for different factors.

## 2.5 Optimal Design

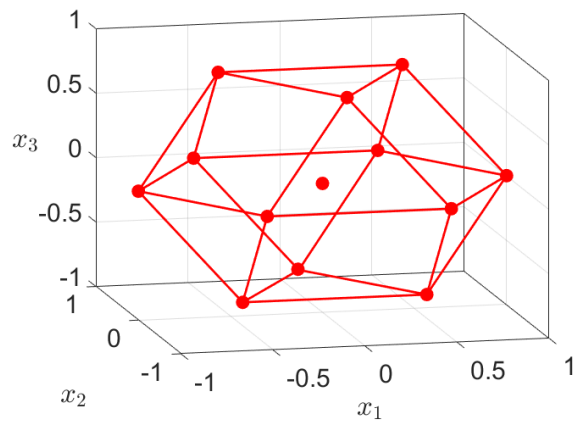
The optimal design, proposed by Kiefer and Wolfowitz [67], is one of the common classical DoE strategy in which the optimality of any design is achieved by minimizing the statistical parameters, such as variance of the predicted responses. Later, a number of optimal criteria were developed by Elfving [83], Kiefer [84], Bondar [85], named as  $\phi$ -optimality criteria. The most common  $\phi$ -optimality criteria are  $D$ ,  $G$ ,  $A$ ,  $E$ ,  $I$ ,  $L$ ,  $c$ ,  $\phi_p$  and integrated mean square error, etc. The advantages of optimal design are that it requires less number of samples than other classical DoE approaches because it involves optimization of the predicted responses. The applications of this strategy can be found in [86–89].

## 2.6 Orthogonal Arrays

The orthogonal array, also known as Taguchi method [69, 90–92], is one of the most popular classical design of experiment schemes. An orthogonal array is expressed as  $OA(N, s_1^{m_1}, s_2^{m_2}, \dots, s_p^{m_p}, \beta)$  of strength  $\beta$  is an  $N \times m$  where  $0 \leq t \leq m$  and  $m = m_1 + m_2 + \dots + m_p$ . Every column (i.e.  $m_i$ ) has  $s_i \geq 2$  elements such that for any strength  $\beta$ , all possible combinations of the elements appeared equally in the matrix. For example,  $OA(4,3,2,2)$  (sometimes expressed as  $OA_4(2^3)$ ) is the  $4/2^3 = 1/2$  fraction of a  $2^3$  full factorial design. Table 2 displays  $OA(4,3,2,2)$  with



(a)



(b)

**Fig. 6** Doehlert design for (a) two and (b) three factors

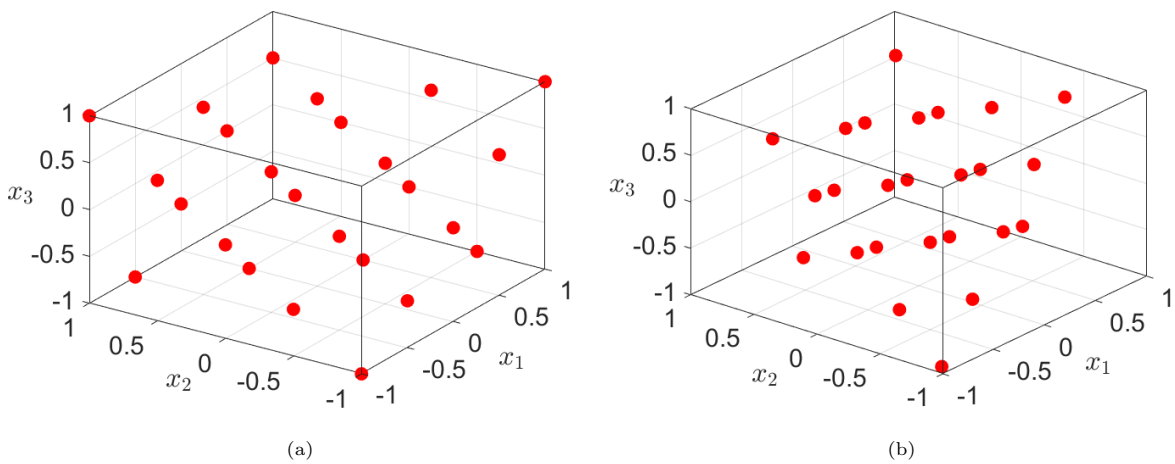
the elements (0,0), (0,1), (1,0) and (1,1) appearing in the matrix only once. The orthogonal array for three factors is shown in Fig. 7.

## 2.7 Random Design

Random design, where the probability of occurrence of all samples is equal, is one of the popular methods for generating random samples. Popular methods under random design are simple random sampling [93, 94], Monte Carlo method (Markov Chain Monte Carlo sampling, Gibbs sampling, Metropolis-Hastings sampling, etc.) [71, 95, 96]. The main drawback of this method is that complete knowledge of the design space is needed. Also, this method shows poor coverage region or clustering for high dimension problems. Fig. 8

**Table 1** A comparison of number of samples generated using factorial, central composite, Box-Behnken and Doehlert design for different factors

No. of Factors	No. of Coefficient	No. of Runs/ Simulations			
		Factorial	CCD	BBD	Doehlert
2	6	9	9	-	7
3	10	27	15	13	13
4	15	81	25	25	21
5	21	243	43	41	31
6	28	729	77	61	43
7	36	2187	143	85	57
8	45	6561	273	113	73

**Fig. 7** (a) Orthogonal array and (b) Orthogonal array-based Latin hypercube design**Table 2** Orthogonal array,  $OA(4, 3, 2, 2)$ 

Row No.	Column No.		
	1	2	3
1	0	0	0
2	0	1	1
3	1	0	1
4	1	1	0

illustrates the Gibbs sampling and the Metropolis-Hasting sampling for two factors.

## 2.8 Quasi-Random Design

The quasi-random design has been widely used as a DoE sampling strategy. The samples generated using this scheme are neither fully random nor regular (like classical DoE schemes). Advantages of a quasi-random design are it uses the flexibility of random sampling techniques as well as the advantages of a grid scheme (as used in classical

DoE designs). The samples using quasi-random design are uniform for high-dimensional problems, and they are also statistically dependent. Various techniques are available for quasi-random design, e.g. Latinized Centroidal Voronoi Tesselation sampling [74, 97], *maximin* Latin Hypercube sampling (LHS) [98–100], Sobol sampling [101–103], Halton sampling [104, 105], Hammersley sampling [106, 107], Faure sampling [79], are commonly used quasi-random design, which are discussed briefly in the next section.

### 2.8.1 Centroidal Voronoi Tesselation Sampling

Centroidal Voronoi tessellation (CVT) is commonly used as a space-filling DoE sampling technique in applied mathematics, engineering and computer science field [74]. In this technique, the



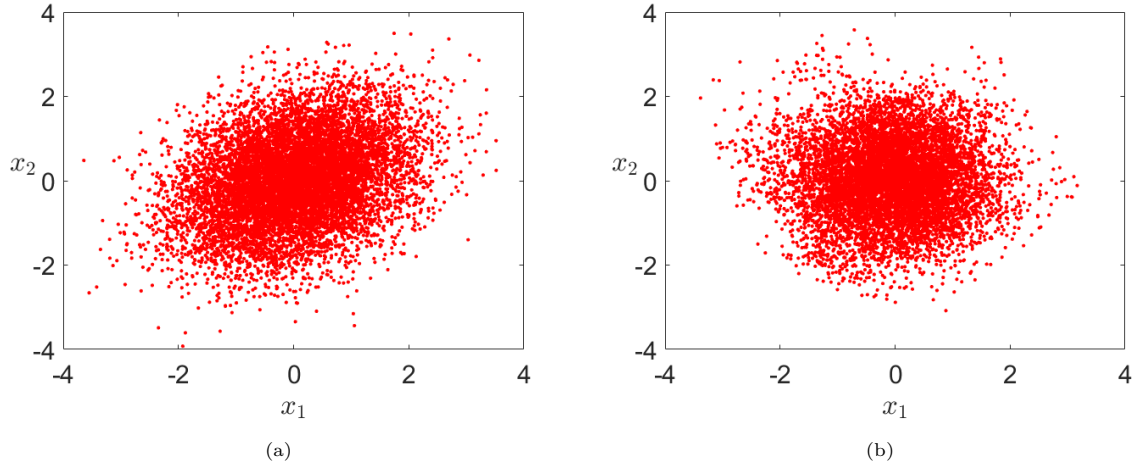


**Fig. 8** (a) Gibbs sampling and (b) Metropolis-Hastings sampling

generators, i.e. a set of points and a distance function, are considered. A Voronoi tessellation is a subset of the points which are closer to one of the generators than other generators [108]. CVT is the tessellation when the generators coincide with the center of the mass of each subset. In general, the generators become the centroids of the Voronoi cell in which the region of the cell is defined by the subset. The algorithm of generating sampling using CVT begins with selecting location of the generators chosen randomly. The actual location of the generators are estimated iteratively and summarized in Algorithm 1. The convergence criteria of this iteration is usually taken as the difference of the centroids obtained in two successive iteration. The samples generated using CVT is shown in Fig. 9(a).

### 2.8.2 Maximin Latin Hypercube Sampling

LHS is a popular DoE sampling strategy [100] for building surrogate models. To generate  $n$  samples using LHS, all  $N$  dimensions are divided into  $n$  equally spaced intervals, and a coordinate value is randomly selected from each interval along a dimension, yielding  $n$  coordinate values in all  $N$  dimensions. Later, a sample point consisting of  $N$  coordinate values is built by randomly selecting one coordinate from each dimension. Thus, a two-dimensional region called the Latin square is formed for every sample. Details of the conventional LHS strategy are shown in Algorithm 2. The

main drawback of LHS is that there is no guarantee that the samples generated cover the entire design space uniformly. For this reason, *maximin* criteria [75], which minimum distance between two samples is maximized, is used during LHS sample generation. Algorithm 3 illustrates the pseudocode for the *maximin* LHS strategy. The samples generated using *maximin* criteria are shown in Fig. 9(b).

### 2.8.3 Sobol Sampling

The Sobol sequence is commonly used quasi-random design, proposed by Sobol [76]. The samples are generated using Sobol sequence are drawn from a special binary fraction ( $v_i^j$ ) of length  $w$  bits where  $i = 1, 2, \dots, w$  and  $j = 1, 2, \dots, N$ .  $N$  is the dimension of the problem. The numbers  $v_i^j$  are known as direction numbers. To generate direction numbers of dimension  $j$ , a primitive polynomial over the field  $F_2$  with elements  $\{0,1\}$  is considered, which is expressed as

$$p_j(x) = x^q + b_1x^{q-1} + \dots + b_{q-1}x + 1 \quad (1)$$

The direction numbers,  $v_i^j$  in the dimension  $j$  are generated using the following recurrence relation, is given by

$$v_i^j = b_1v_{i-1}^j \oplus b_2v_{i-2}^j \oplus \dots \oplus b_{q-1}v_{i-(q-1)}^j \oplus v_{i-q}^j \oplus (v_{i-q}^j/2^q); \quad i > q \quad (2)$$

**Algorithm 1** Pseudo-code for generation of CVT Sampling [108]

- 
- 1: Aim: Generate  $n$  samples over the  $N$ -dimensional space which are located at centroids of the centroidal Voronoi tessellation.
  - 2: Define the number of iteration ( $N_{Iter}$ ) and the number of random points generated in every iteration ( $m$ ).
  - 3: Set the parameters  $\alpha_1$ ,  $\alpha_2$ ,  $\beta_1$  and  $\beta_2$  which define how the centroids are updated in every iteration. Also,  $\alpha_2, \beta_2 > 0$ ,  $\alpha_1 + \alpha_2 = 1$  and  $\beta_1 + \beta_2 = 1$ .
  - 4: Choose an initial set of random samples,  $x_i$ ,  $i = 1, 2, \dots, n$  which are assumed centroids over the domain.
  - 5: Set  $p_i = 1$ ,  $i = 1, 2, \dots, n$ , which represents the number of times every centroid is updated.
  - 6: **Begin**
  - 7: **for** Iteration = 1 to  $N_{Iter}$  **do**
  - 8:     Generate the random samples  $y_k$ ,  $k = 1, 2, \dots, m$  according to pre-defined probability density function,  $\rho(\mathbf{x})$
  - 9:     **for**  $i = 1$  to  $n$  **do**
  - 10:         Collect the set  $W_i$  of all sample  $y_k$  which are closest to  $x_i$  and estimate their mean  $u_i$ .
  - 11:         **if**  $W_i = \phi$  (i.e. null set) **then**
  - 12:             Do nothing
  - 13:         **else**
  - 14:             Update the centroid,  $x_i$  as,
$$x_i = \frac{(\alpha_1 p_i + \beta_1)x_i + (\alpha_2 p_i + \beta_2)u_i}{p_i + 1}, \quad p_i = p_i + 1$$
  - 15:         **end if**
  - 16:     **end for**
  - 17:     If the convergence criteria is satisfied i.e., the difference of centroids obtained in two successive iteration is less than tolerance, terminate.
  - 18: **end for**
- 

**Algorithm 2** Pseudo-code for generation of basic Latin Hypercube Sampling

- 
- 1: Aim: Generate  $n$  samples over the  $N$ -dimensional space.
  - 2: Let  $x_{ij}$  is the  $j$ -th coordinate of the  $i$ -th sample,  $x_i$ .
  - 3: **Begin**
  - 4: **for**  $j = 1$  to  $N$  **do**
  - 5:     Generate  $P_j$ , a random permutation of the set  $\{1, \dots, n\}$ .
  - 6: **end for**
  - 7: **for**  $j = 1$  to  $N$  **do**
  - 8:     **for**  $i = 1$  to  $n$  **do**
  - 9:         Generate  $x_{ij} = \frac{P_j(i) - U_j(i)}{n}$ , where  $U_j$  is the uniform random number in between  $[0, 1]$ .
  - 10:     **end for**
  - 11: **end for**
- 

Sobol sequence is written as

$$x_n^j = a_1 v_1^j \oplus a_2 v_2^j \oplus \dots \oplus a_w v_w^j \quad (3)$$

where  $n = \sum_{i=0}^w a_i 2^i$ . The coefficient  $a_i$  is the random number in between  $\{0, 1\}$ . Fig. 9(c) illustrates the samples generated using the Sobol sequence.

**2.8.4 Halton Sampling**

The Halton sampling, proposed by Halton [77], is quasi-random designs. Consider, first  $N$  prime numbers as  $m_1, m_2, \dots, m_N$ . The Halton sequence for  $N$ -dimensional space can be expressed as

$$x_n = \left( \Phi_{m_1}(n), \dots, \Phi_{m_i}(n), \dots, \Phi_{m_N}(n) \right) \quad (4)$$

In the above equation, the notation  $\oplus$  represents the bitwise XOR. Finally, in the dimension  $j$ , the

**Algorithm 3** Pseudo-code for generation of Maximin Latin Hypercube Sampling [109]

- 
- 1: Aim: Generate  $n$  samples over the  $N$ -dimensional space in which the minimum distance between samples are maximized.
  - 2: Define the number of iteration ( $N_{Iter}$ ) and the number of interchanges for every iteration ( $m$ ).
  - 3: **Begin**
  - 4: **for** Iteration = 1 to  $N_{Iter}$  **do**
  - 5:   Generate  $n$  samples using basic Latin hypercube sampling, shown in Algorithm 2.
  - 6:   Assume  $p_1$  and  $p_2$  are the indices of samples with minimum distance.
  - 7:   **for**  $i = 1$  to  $m$  **do**
  - 8:     Select index random either  $p_1$  or  $p_2$ .
  - 9:     For a random integer,  $r_{col}$  in  $[1, \dots, N]$ , and a random row,  $r_{row}$  in  $[1, \dots, n]$ , interchange the values in column  $r_{col}$ , rows index and  $r_{row}$ .
  - 10:     If the minimum distance of samples is increased, accept the interchanges and update the values of  $p_1$  and  $p_2$ .
  - 11:   **end for**
  - 12:   If the minimum distance between samples is smaller than previous iteration, terminate.
  - 13: **end for**
- 

where  $\Phi_{m_i}(n)$  is the  $i$ -th radical inverse function, which is expressed in the mathematical form as

$$\Phi_{m_i}(n) = \sum_{j=0}^{l(i)} a_j(i, n) m_i^{-(j+1)} \quad (5)$$

In the above equation,  $a_j$  is the integer coefficient, and it is given as  $a_j(i, n) \in [0, m_i - 1]$ . Also, the integer terms  $n$  and  $l$  are given by

$$n = \sum_{j=0}^{l(i)} a_j(i, n) m_i^j, \quad l(i) = \lceil \log_{m_i} n \rceil \quad (6)$$

The samples generated using the Halton sequence are only bounded in between  $[0,1]^N$  which are spread more evenly within the design space compared to random sampling. Fig. 9(d) shows the samples generated using the Halton sequence. It is noted that the samples in Fig. 9(d) are scaled considering the bound  $[-1,1]$ .

### 2.8.5 Hammersley Sampling

The Hammersley sampling is a popular quasi-random design, similar to the Halton sequence. The Hammersley sequence differs from the Halton sequence in that the Hammersley sequence employs  $(N-1)$ ,  $\Phi$  sequence. The Hammersley

sequence for  $N$ -dimensional space is expressed as

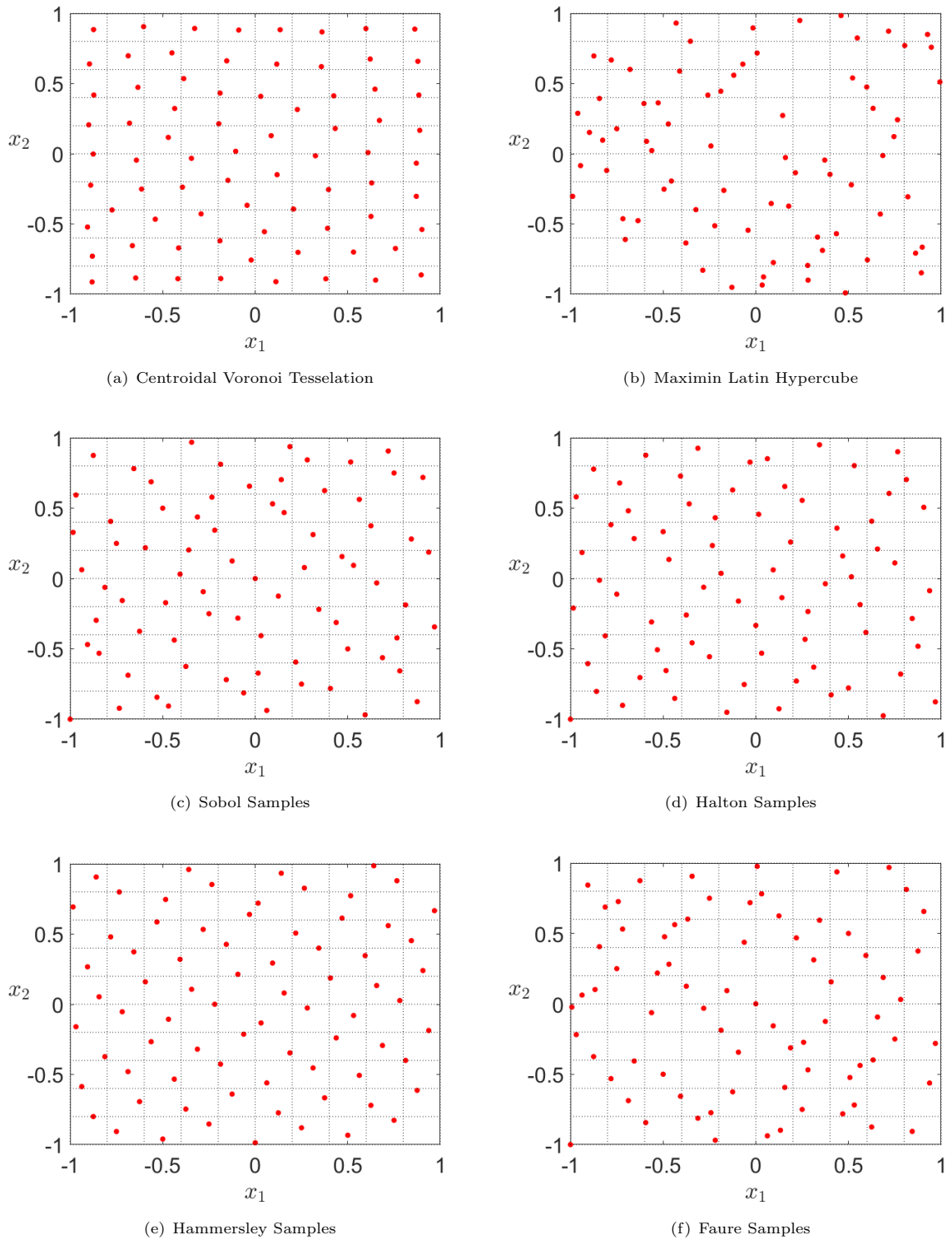
$$x_n = \left( \frac{n}{N}, \Phi_{m_1}(n), \dots, \Phi_{m_i}(n), \dots, \Phi_{m_{N-1}}(n) \right) \quad (7)$$

The primary distinction between the Halton and Hammersley sequences is that the Halton sequence can generate an infinite number of samples (i.e., infinite  $N$ ), whereas the Hammersley sequence requires an upper bound on the number of samples. Fig. 9(e) shows the samples generated using the Hammersley sequence.

### 2.8.6 Faure Sampling

The Faure sequence, which is similar to the Halton sequence, proposed by Faure [79], is a well-known quasi-random sample generation technique. Consider,  $m$  is the first prime number such that  $m \geq n$ , where  $n$  is the total number of samples. Also, the upper bound of the sample size is  $m^p$ . This is the main difference between the Faure and the Halton sequences. For example, if  $n = 50$  i.e., 50 samples are required to generate, the last Halton sequence (i.e., in dimension 50) uses the 50-th prime number, which is 229, whereas the Faure sequence uses the first prime number after 50. The main advantage of using Faure sampling over Halton sampling is that the Faure sequence is faster to fill the gaps for high dimensional problems. Also, it prevents correlation problems in high dimensions, which are seen in the Halton sequence.

## State-of-the-Art Review of Design of Experiments for PINN

**Fig. 9** Various sampling strategies for quasi-random design

Let  $c_{ij} = \binom{i}{j} \pmod{m}$  where  $0 \leq j \leq i \leq p$ . This implies  $\{c_{ij} - \binom{i}{j}\}$  is the multiple of  $m$ . The base  $m$  representation of  $n$  is expressed as

$$n = \sum_{i=0}^{p-1} a_i(n) m^i \quad (8)$$

where the coefficients  $a_i \in [0, m)$  takes the integer values. The samples produced by the Faure sequence are denoted by

$$x_n = \sum_{j=0}^{p-1} a_j(n) m^{-(j+1)} \quad (9)$$

where the coefficient  $a_j = \sum_{l=j}^{p-1} c_{lj} a_l(n) \pmod{p}$ ,  $j \in \{0, 1, \dots, p-1\}$ . Fig. 9(f) shows the samples generated using the Faure sequence.

## 2.9 Full Grid Design

Full grid design, also known as the collocation technique, is a well established scheme for generating sample points [110–112]. In this study, a Lagrangian polynomial is used for the interpolation. Let,  $x_i^j$  be the support nodes which are expressed as  $x_i^j \in x^j = \{x_1^j, x_2^j, \dots, x_{n_j}^j\} \in [-1, 1]$  be a sequence of abscissas for Lagrange interpolation on  $[-1, 1]$ . The collocation method is based on one-dimensional Lagrange polynomial interpolation at  $N$  Gauss quadrature points and is expressed as

$$\mathcal{U}^j(y) = \sum_{i=1}^{n_j} y(x_i^j) \cdot \mathcal{L}_i^j(x) \quad (10)$$

where  $n_j$  is the total number of grid points. Also, in the above equation,  $\mathcal{L}$  is the Lagrange polynomial, given by

$$\mathcal{L}_i^j(x) = \prod_{k=1, k \neq i}^{n_j} \left( \frac{x - x_k^j}{x_i^j - x_k^j} \right) \quad (11)$$

Eq. 10 defines the one-dimensional problem. For multi-variate cases, the full tensor product interpolation is written as

$$\begin{aligned} \mathcal{I}^\beta \mathcal{U}(y) &= \left( \mathcal{U}^{j_1} \otimes \mathcal{U}^{j_2} \otimes \dots \otimes \mathcal{U}^{j_\beta} \right)(y) \\ &= \sum_{i_1=1}^{n_1} \sum_{i_2=1}^{n_2} \dots \sum_{i_\beta=1}^{n_\beta} y(\mathbf{x}_{i_1}^{j_1}, \mathbf{x}_{i_2}^{j_2}, \dots, \mathbf{x}_{i_\beta}^{j_\beta}) \\ &\quad \left( \mathcal{L}_{i_1}^{j_1}(\mathbf{x}) \otimes \mathcal{L}_{i_2}^{j_2}(\mathbf{x}) \otimes \dots \otimes \mathcal{L}_{i_\beta}^{j_\beta}(\mathbf{x}) \right) \end{aligned} \quad (12)$$

where  $\beta$  is the dimension of the problem. Fig. 10 illustrates the grid points generated using the collocation technique for various levels ( $\mu$ ) of sparse grid for two and three random variables.

## 2.10 Sparse Grid Design

The sparse grid scheme has been proven an efficient scheme for generating support points [113]. In this study, Smolyak's algorithm [114] is utilized to generate sampling, based on the hierarchical sampling scheme [115]. The samplings generated from previous interpolation depth are used in the subsequent interpolation to produce the new sampling set. The sparse grid ( $\mathcal{SG}$ ) can be formulated as

$$\mathcal{SG}_\mu = \sum_{\sum_{i=1}^{\beta} j_i \leq \mu + \beta - 1} \left( \Delta^{j_1} \otimes \Delta^{j_2} \otimes \dots \otimes \Delta^{j_\beta} \right)(y) \quad (13)$$

where  $\mu$  is the level of the sparse grid design and  $\beta$  denotes the dimension of the problem, i.e., the number of variables considered. In Eq. 13, the difference function,  $\Delta^j$  equals to  $(\mathcal{U}^j - \mathcal{U}^{j-1})$  where  $\mathcal{U}$  is the interpolation function for the univariate case. The unidimensional interpolation function can be expressed using quadrature form, is given by

$$\mathcal{U}^j(y) = \sum_{i=1}^{n_j} y(x_i^j) \cdot \check{A}_i^j(x) \quad (14)$$

In the above equation,  $n_j$  denotes the number of grid points for a given random parameter. Also,  $\check{A}_i^j$  is the basis function, which is  $\check{A}_i^j \in \mathcal{C}([-1, 1])$ ,  $\check{A}_i^j(x_k^j) = \delta_{ik}$ . Here,  $x_i^j$  are the support nodes, which are expressed as  $x_i^j \in x^j = \{x_1^j, x_2^j, \dots, x_{n_j}^j\}$  and  $x_k^j \in [-1, 1]$ ,  $1 \leq k \leq n_j$ . The interpolation function for the univariate case, defined in Eq. 14,

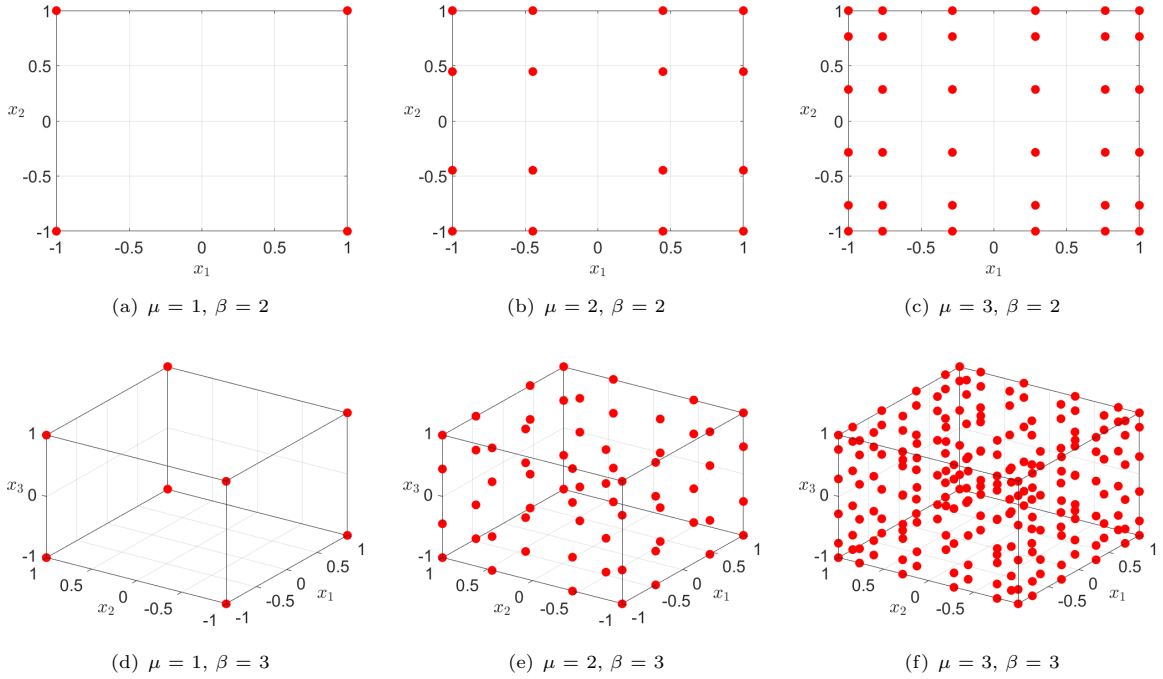


**Fig. 10** Full tensor product grid for different levels for two and three factors

can be extended to the multivariate case as:

$$\begin{aligned} & (\mathcal{U}^{j_1} \otimes \mathcal{U}^{j_2} \otimes \dots \otimes \mathcal{U}^{j_\beta})(y) \\ &= \sum_{i_1=1}^{n_1} \sum_{i_2=1}^{n_2} \dots \sum_{i_\beta=1}^{n_\beta} y(\mathbf{x}_{i_1}^{j_1}, \mathbf{x}_{i_2}^{j_2}, \dots, \mathbf{x}_{i_\beta}^{j_\beta}). \quad (15) \\ & \quad \left( \check{A}_{i_1}^{j_1}(\mathbf{x}) \otimes \check{A}_{i_2}^{j_2}(\mathbf{x}) \otimes \dots \otimes \check{A}_{i_\beta}^{j_\beta}(\mathbf{x}) \right) \end{aligned}$$

The sparse grid interpolation presented above uses two types of basis functions, i.e., piecewise linear and polynomial basis functions. In this study, the Chebyshev-Gauss-Lobatto grid [116] is used, which is one of the most commonly used polynomial grids (i.e., higher order basis functions are considered) and provides the higher accuracy. In the Chebyshev-Gauss-Lobatto grid scheme, the total number of grid points for each random variable and grid points are given as:

$$n_j = \begin{cases} 1, & \text{if } j = 1 \\ 2^{j-1} + 1, & \text{if } j > 1 \end{cases} \quad (16a)$$

$$x_i^j = -\cos \frac{\pi(i-1)}{n_j-1}, \quad i = 1, 2, \dots, n_j \quad (16b)$$

Also, in Eq. 15, the basis function,  $\check{A}_i^j$  is given by

$$\check{A}_i^j = \begin{cases} \frac{2}{n_j-1} \left[ 1 - \frac{\cos(\pi(i-1))}{n_j(n_j-2)} - \right. \\ \quad \left. 2 \sum_{k=1}^{(n_j-3)/2} \frac{1}{4k^2-1} \cdot \cos \frac{2\pi k(i-1)}{n_j-1} \right], & \text{for } i = 2, \dots, (n_j-1) \\ \frac{1}{n_j(n_j-2)}, & \text{for } i = 1 \& n_j \end{cases} \quad (17)$$

Fig. 11 shows the grid points generated using a sparse grid scheme for various levels ( $\mu$ ) of sparse grid for two and three random variables.

## 2.11 Rotational Sparse Grid Design

Recently, rotational sparse grid design has been developed as one of the efficient design of experiment schemes, proposed by Wu *et al.* [117]. In this method, the initial support points are generated through a sparse grid scheme, as mentioned in Section 2.10. To obtain maximum information from those support points, an optimization has been performed by rotating all support points with a fixed angle of rotation. The rotational

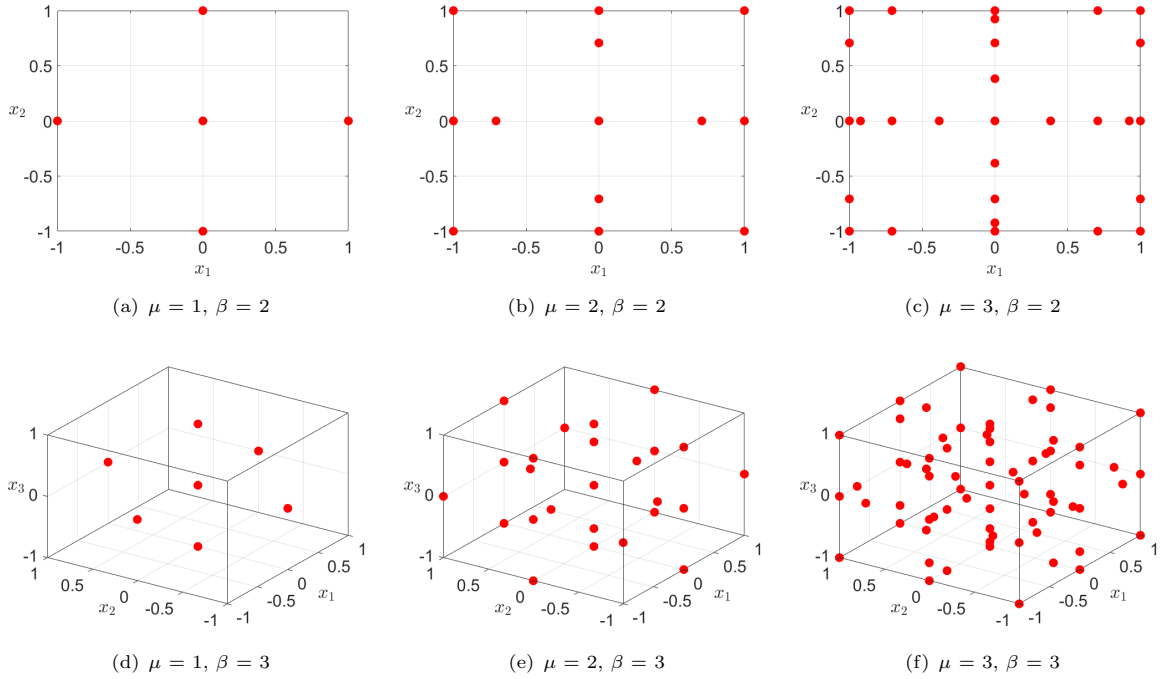


**Fig. 11** Grid points generated using sparse grid scheme

matrix is given by for the two-dimensional problem as:

$$\mathcal{R}(\theta) = \begin{bmatrix} \cos \theta & -\sin \theta \\ \sin \theta & \cos \theta \end{bmatrix} \quad (18)$$

where  $\theta$  is the angle of rotation. Similarly, for three-dimensional problems, the rotational matrix is written as:

$$\mathcal{R}_x(\theta) = \begin{bmatrix} 1 & 0 & 0 \\ 0 & \cos \theta & -\sin \theta \\ 0 & \sin \theta & \cos \theta \end{bmatrix} \quad (19a)$$

$$\mathcal{R}_y(\theta) = \begin{bmatrix} \cos \theta & 0 & \sin \theta \\ 0 & 1 & 0 \\ -\sin \theta & 0 & \cos \theta \end{bmatrix} \quad (19b)$$

$$\mathcal{R}_z(\theta) = \begin{bmatrix} \cos \theta & -\sin \theta & 0 \\ \sin \theta & \cos \theta & 0 \\ 0 & 0 & 1 \end{bmatrix} \quad (19c)$$

In the above equation,  $\mathcal{R}_x(\theta)$  is the rotational matrix where the rotation is performed with respect to the x-axis. Similarly,  $\mathcal{R}_y(\theta)$  and  $\mathcal{R}_z(\theta)$  are the rotational matrix for rotations about the y- and z-axes, respectively. For  $n$ -dimensional

problem, the rotational matrix is given by

$$\mathcal{R}(\theta) = \begin{bmatrix} 1 & \dots & 0 & \dots & 0 & \dots & 0 \\ \vdots & \ddots & \vdots & \ddots & \vdots & \ddots & \vdots \\ 0 & \dots & \cos \theta & \dots & -\sin \theta & \dots & 0 \\ \vdots & \ddots & \vdots & \ddots & \vdots & \ddots & \vdots \\ 0 & \dots & \sin \theta & \dots & \cos \theta & \dots & 0 \\ \vdots & \ddots & \vdots & \ddots & \vdots & \ddots & \vdots \\ 0 & \dots & 0 & \dots & 0 & \dots & 0 \end{bmatrix} \begin{matrix} i\text{-th} \\ j\text{-th} \\ k\text{-th} \\ i\text{-th} \\ j\text{-th} \\ k\text{-th} \end{matrix} \quad (20)$$

The support points on  $j$ -th and  $k$ -th axes are rotated with respect to the  $i$ -th axis in this case. The grid points using a sparse grid scheme are shown in Fig. 12 for a two-dimensional problem. The angle of rotation ( $\theta$ ) is estimated by performing the optimization problem considering some objective functions from the designer's perspective.

### 3 Machine Learning

Machine learning is categorized into four groups, i.e., supervised learning, unsupervised learning,

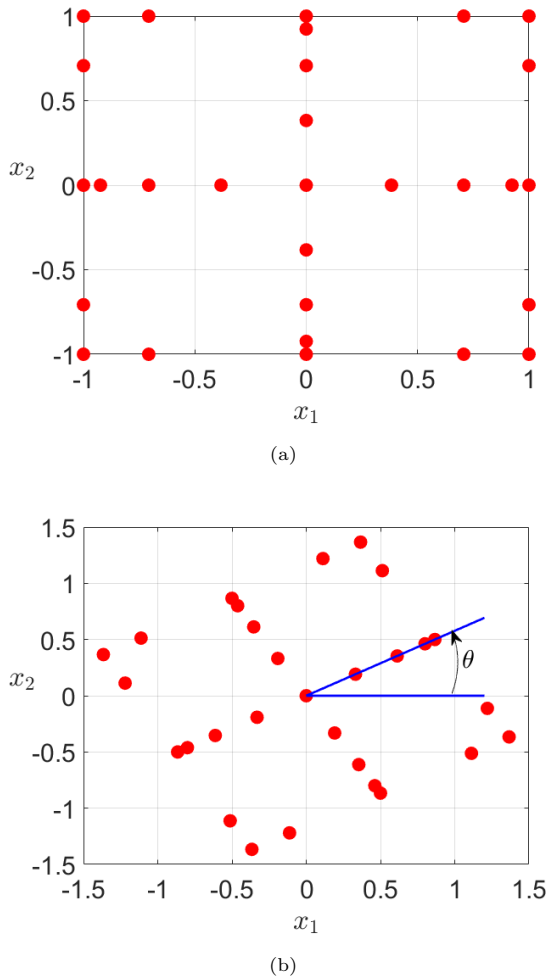


**Fig. 12** Support points generated using (a) sparse grid and (b) rotational sparse grid scheme for two dimensional problem

semi-supervised learning, and reinforcement learning. Supervised learning is used to develop the predicted models where there is a mapping between the set of input vectors and one or more outputs. Regression and classification problems belong to supervised learning. Unsupervised learning is used to estimate the probability distribution of the provided data. Prediction using this algorithm is not possible because the data is not labeled. Clustering is an example of unsupervised learning. Semi-supervised learning is the combination of supervised and unsupervised learning where few samples are labelled (i.e., supervised) and unsupervised learning is used to enhance the performance of supervised learning. Finally, the

reinforced learning interacts with the environment to learn the behaviour of the decision variable by enhancing the expected average reward [118]. Fig. 13 illustrates the applications of machine learning in the science and engineering fields.

### 3.1 Feed-Forward Neural Networks

Artificial neural networks belong to the supervised learning class, which mimics the neurons of the brain. Generally, it is a mapping between input and output vectors. It consists of at least three layers, i.e., the input layer, the hidden layer, and the output layer. As the information propagates from the input layer through hidden layers to the output layer, it is known as feed-forward neural networks. When more than one hidden layer is used, the network is called “deep” neural network. In each hidden layer, one or more neurons are used. A schematic diagram of the architecture of the neural network is shown in Fig. 14. The output of the network is a linear combination of the neurons, which is related to the weight of the connection, called synaptic weight, and a transfer function, called the activation function.

From Fig. 14,  $\mathbf{x} = [x_1, x_2, \dots, x_n]$  are the  $n$  input variables. The output of a neuron is estimated to be two steps. Firstly, the input vector  $\mathbf{x}$  is transformed into a linear combination, i.e.,

$$z = \mathbf{w}^T \mathbf{x} + b \quad (21)$$

where  $\mathbf{w}$  is the synaptic weight and  $b$  is the bias. Second, the neuron output  $a(\mathbf{x})$  is estimated by feeding  $z$  into an activation function,  $\sigma$ , in order to obtain the data’s nonlinearity, which is given as

$$a(\mathbf{x}) = \sigma(z) \quad (22)$$

The common activation functions used in neural networks are tabulated in Table 3. For accurate prediction of the output response ( $y$ ), each synaptic weight in each layer needs to be updated. The backpropagation learning algorithm is used for updating the weights. In that case, the loss function ( $\mathcal{L}$ ) is taken into account and must be minimized. The commonly used loss functions are tabulated in Table 4. The stochastic gradient



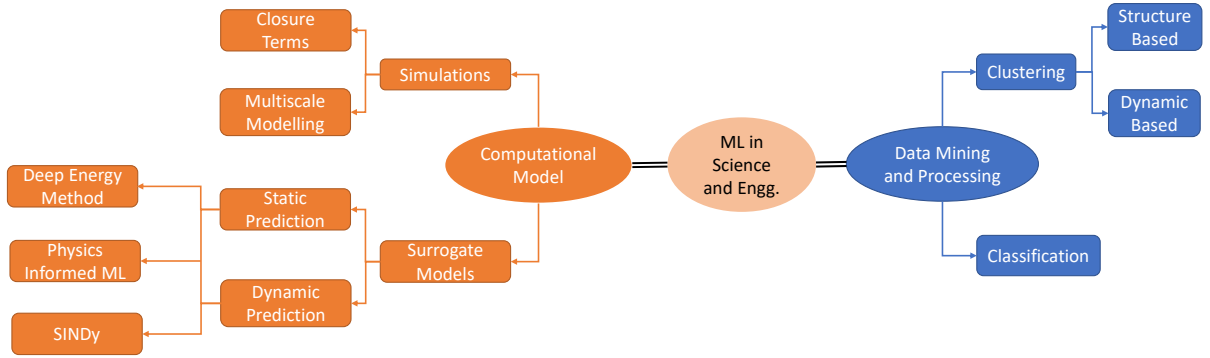


**Fig. 13** An overview of applications of machine learning

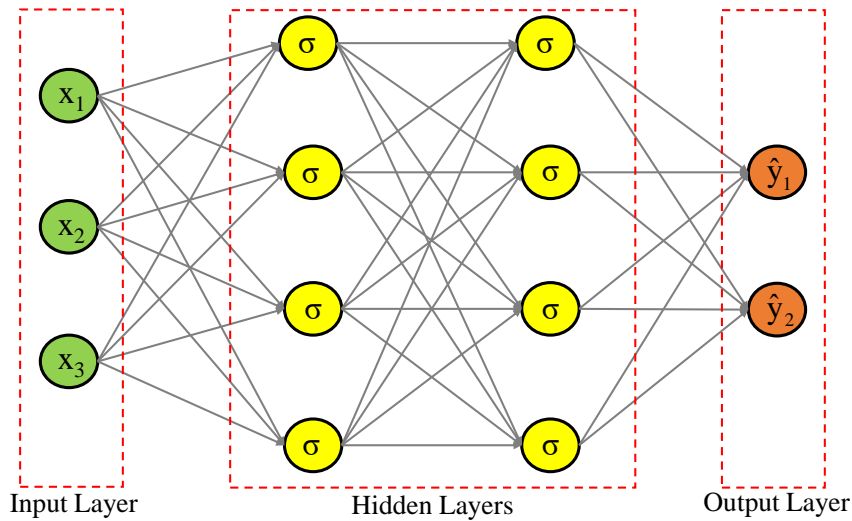


**Fig. 14** Basic architecture of feed-forward neural network

descent technique is used to solve the minimization problem, which is expressed as

$$[\mathbf{w}]^o = [\mathbf{w}]^{o-1} - \eta \frac{\partial \mathcal{L}}{\partial \mathbf{w}} \quad (23)$$

where  $o$  is the current iteration and  $\eta$  represents the learning rate.

### 3.2 Physics-Informed Neural Network

A physics-informed neural network (PINN) is a special class of feed-forward neural network where physical conditions are imposed on the neural network as a loss function. The data-driven neural network, as discussed in Section 3.1, is often cost-effective for a complex physical system where a large amount of solution data is required. PINN

is used to solve problems where only a few data points are available, such as noisy data from an experiment. To estimate the accurate solution of the physical system, the physical laws of the governing system are imposed on the network. To illustrate the algorithm of PINN, a nonlinear partial differential equation is considered, which is expressed in the following form

$$\frac{\partial u}{\partial t} + \mathcal{N}[u; \lambda] = 0; \quad x \in \Omega, t \in \mathcal{T} \quad (24)$$

The latent solution in the above equation is  $u(x, t)$ , which is a function of time  $t \in [0, T]$  and a spatial variable  $x \in \Omega$ , where  $\Omega$  represents a space in  $\mathbb{R}^D$ . Also, in Eq. 24,  $\mathcal{N}[u; \lambda]$  denotes a non-linear differential operator with coefficients  $\lambda$ . Like in feed-forward neural networks, the weights

## State-of-the-Art Review of Design of Experiments for PINN

**Table 3** Common activation functions used in neural networks

No.	Activation Function	Equation	Range
1	Aranda [119]	$\sigma(x) = 1 - (1 + 2e^x)^{-1/2}$	[0, 1]
2	Bi-sig1 [120]	$\sigma(x) = 0.5 \left( \frac{1}{1+e^{-x+1}} + \frac{1}{1+e^{-x-1}} \right)$	[0, 1]
3	Bi-sig2 [120]	$\sigma(x) = 0.5 \left( \frac{1}{1+e^{-x}} + \frac{1}{1+e^{-x-1}} \right)$	[0, 1]
4	Bi-tanh1 [120]	$\sigma(x) = 0.5 \left[ \tanh\left(\frac{x}{2}\right) + \tanh\left(\frac{x+1}{2}\right) \right] + 0.5$	[-0.5, 1.5]
5	Bi-tanh2 [120]	$\sigma(x) = 0.5 \left[ \tanh\left(\frac{x-1}{2}\right) + \tanh\left(\frac{x+1}{2}\right) \right] + 0.5$	[-0.5, 1.5]
6	Cloglog [121]	$\sigma(x) = 1 - e^{-e^x}$	[0, 1]
7	Cloglogm [122]	$\sigma(x) = 1 - 2e^{-0.7e^x} + 0.5$	[-0.5, 1.5]
8	Elliott [123]	$\sigma(x) = \frac{0.5x}{1+x} + 0.5$	[0, 1]
9	ELU	$\sigma(x) = \begin{cases} \alpha(e^x - 1), & x < 0 \\ x, & x \geq 0 \end{cases}$	$[-\infty, +\infty]$
10	Gaussian	$\sigma(x) = e^{-x^2}$	[0, 1]
11	Heaviside	$\sigma(x) = \begin{cases} 0, & x < 0 \\ 0.5, & x = 0 \\ 1, & x > 0 \end{cases}$	$[-\infty, +\infty]$
12	Hyperbolic Tangent	$\sigma(x) = \frac{e^x - e^{-x}}{e^x + e^{-x}}$	$[-\infty, +\infty]$
13	Linear	$\sigma(x) = x$	$[-\infty, +\infty]$
14	Logarithmic	$\sigma(x) = \begin{cases} \ln(1+x) + 0.5, & x \geq 0 \\ -\ln(1-x) + 0.5, & x < 0 \end{cases}$	$[-\infty, +\infty]$
15	Loglog [122]	$\sigma(x) = e^{-e^{-x}} + 0.5$	[0.5, 1.5]
16	Logsigm [124]	$\sigma(x) = \left( \frac{1}{1+e^{-x}} \right)^2 + 0.5$	[0.5, 1.5]
17	Log-sigmoid	$\sigma(x) = \frac{1}{1+e^{-x}}$	[0, 1]
18	Modified Elliott [125]	$\sigma(x) = \frac{x}{\sqrt{1+x^2}} + 0.5$	[-0.5, 1.5]
19	Piece-wise Linear	$\sigma(x) = \begin{cases} 1, & x \geq 0.5 \\ x + 0.5, & -0.5 < x < 0.5 \\ 0, & x \leq -0.5 \end{cases}$	$[-\infty, +\infty]$
20	PReLU	$\sigma(x) = \begin{cases} \alpha x, & x < 0 \\ x, & x \geq 0 \end{cases}$	$[-\infty, +\infty]$
21	ReLU	$\sigma(x) = \begin{cases} 0, & x < 0 \\ x, & x \geq 0 \end{cases}$	$[-\infty, +\infty]$
22	Rootsig [126]	$\sigma(x) = \frac{x}{1+\sqrt{1+x^2}} + 0.5$	[-0.5, 1.5]
23	Saturated	$\sigma(x) = \frac{x+1-x-1}{2} + 0.5$	[-0.5, 1.5]
24	Sech	$\sigma(x) = \frac{2}{e^x + e^{-x}}$	[0, 1]
25	Sign	$\sigma(x) = \begin{cases} -1, & x < 0 \\ 0, & x = 0 \\ 1, & x > 0 \end{cases}$	$[-\infty, +\infty]$
26	Sigmoidalm [124]	$\sigma(x) = \left( \frac{1}{1+e^{-x}} \right)^4 + 0.5$	[0.5, 1.5]
27	Sigmoidalm2 [127]	$\sigma(x) = \left( \frac{1}{1+e^{-x/2}} \right)^4 + 0.5$	[0.5, 1.5]
28	Sigt [128]	$\sigma(x) = \frac{1}{1+e^{-x}} + \frac{1}{1+e^{-x}} \left( 1 - \frac{1}{1+e^{-x}} \right)$	[0, 1]
29	Skewed-sig [129]	$\sigma(x) = \left( \frac{1}{1+e^{-x}} \right) \left( \frac{1}{1+e^{-2x}} \right) + 0.5$	[0.5, 1.5]
30	Softplus	$\sigma(x) = \ln(1 + e^x)$	$[-\infty, +\infty]$
31	Softsign [123]	$\sigma(x) = \frac{x}{1+x} + 0.5$	[-0.5, 1.5]
32	Wave [130]	$\sigma(x) = (1 - x^2)e^{-x^2}$	[-0.055, 1]

**Table 4** Common loss functions used in neural networks for regression analysis

No.	Loss Function	Equation
1	Mean absolute loss	$y - \hat{y}_1$
2	Mean squared loss	$y - \hat{y}_2^2$
3	Expectation loss	$y - p(\hat{y})_1$
4	Regularised expectation loss	$y - p(\hat{y})_2^2$
5	Chebyshev loss	$\max_j   p(\hat{y})^{(j)} - y^{(j)}  $
6	Hinge loss	$\sum_j \max\left(0, \frac{1}{2} - y^{(j)} \hat{y}^{(j)}\right)$
7	Squared hinge loss	$\sum_j \max\left(0, \frac{1}{2} - y^{(j)} \hat{y}^{(j)}\right)^2$
8	Cubed hinge loss	$\sum_j \max\left(0, \frac{1}{2} - y^{(j)} \hat{y}^{(j)}\right)^3$
9	Cross entropy loss	$-\sum_j y^{(j)} \log p(\hat{y})^{(j)}$
10	Squared log loss	$-\sum_j \left[ y^{(j)} \log p(\hat{y})^{(j)} \right]^2$
11	Tanimoto loss	$-\frac{\sum_j p(\hat{y})^{(j)} y^{(j)}}{p(\hat{y})_2^2 + y_2^2 - \sum_j p(\hat{y})^{(j)} y^{(j)}}$
12	Cauchy-Schwarz Divergence	$-\log \frac{\sum_j p(\hat{y})^{(j)} y^{(j)}}{p(\hat{y})_2 y_2}$

$y$  and  $\hat{y}$  represent true and predicted value

$j$  represents the dimension of a given vector

$p(\cdot)$  is the probability estimate

and bias in PINN are estimated by minimizing a cost function, which is given as

$$\mathcal{L} = \mathcal{L}_u + \mathcal{L}_f \quad (25)$$

where  $\mathcal{L}_u$  and  $\mathcal{L}_f$  denote the residual of a PDE (i.e., mean square error between  $u(x, t)$  and  $\hat{u}(x, t)$ ) and the residual corresponding to initial and boundary conditions, respectively. PINN is used for either data-driven interference or data-driven identification of differential equations. Data-driven interference is a forward problem in which  $\lambda$  of the differential equation (Eq. 24) is known and  $u(x, t)$  is solved based on initial and boundary conditions, whereas data-driven identification identifies coefficients  $\lambda$  of the differential equation based on scattered data of the solution  $u(x, t)$ . A schematic diagram of PINN is shown in Fig. 15.

## 4 Numerical Results

In this section, numerical examples are presented to illustrate the performance of a PINN considering various design experiment schemes to generate

the training data-set. For this purpose, five different nonlinear differential equations are considered, i.e., Viscous Burger's equation, Schrödinger equation, one-dimensional heat equation, Allen-Cahn equation and Korteweg-de Vries equation. The neural network is designed to solve those PDEs, which approximates the true solution  $u(t, x)$ , denoted by  $\hat{u}(t, x)$ . The number of neurons in the hidden layers is constant for a given problem. The total number of hidden layers and the number of neurons in each hidden layer are obtained by comparing the prediction responses using a neural network with the actual solution multiple times. The hyperbolic tangent tanh is used as an activation function for every neuron and this is same for all problems. To train the neural network, different DoE schemes are used, i.e., factorial design (FD), central composite design (CCD), centroidal Voronoi tessellation (CVT), maximin Latin hypercube sampling (MLH), Sobol sampling, Halton sampling, Hammersley sampling, Faure sampling, full grid design (FGD), and sparse grid design (SGD). The accuracy of the predicted responses using a neural network depends on the number of DoE samples in the training set. Therefore, preliminary study is devoted to its accuracy by carrying out the

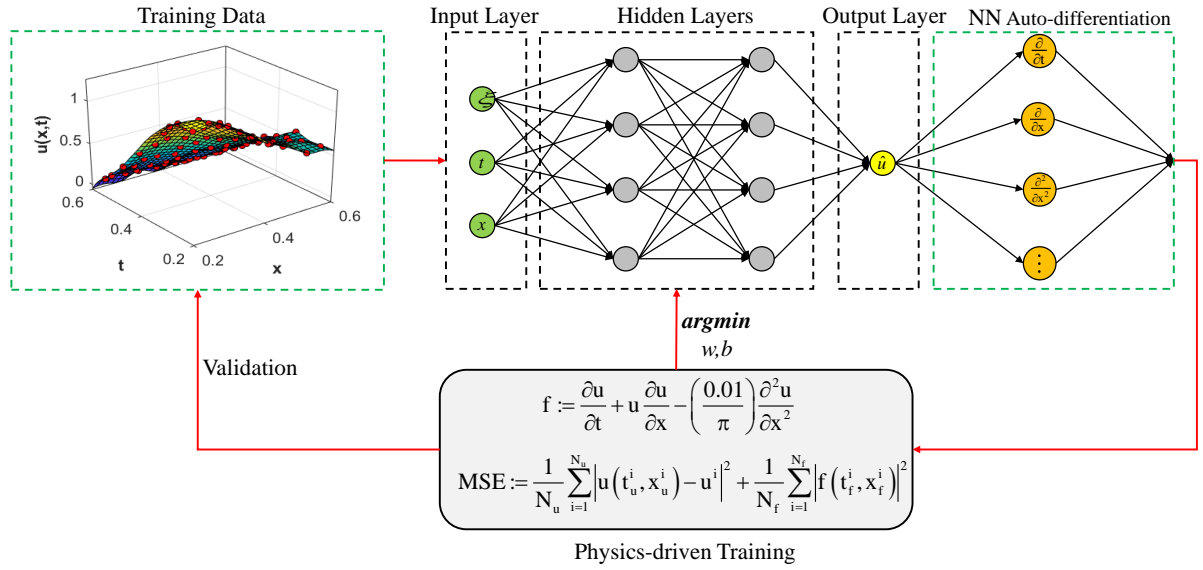


**Fig. 15** Schematic diagram of physics informed neural network

simulation considering increasing size of the training set (i.e., from 50 to 500 with a step size of 50). The accuracy is evaluated using the mean squared error (MSE) between actual and predicted responses. For the simulation purposes, `python` using `TensorFlow` [131] and `SciANN` [132], `MATLAB` softwares are used.

#### 4.1 Problem 1: Viscous Burger's Equation

As the first example, viscous Burger's equation is illustrated, whose applications are seen in the fluid mechanics, acoustics, and traffic flow fields [133]. The governing PDE equation for viscous Burger's equation is given by [134]

$$\frac{\partial u}{\partial t} + u \frac{\partial u}{\partial x} - \nu \frac{\partial^2 u}{\partial x^2} = 0 \quad (26)$$

where  $(x, t) \in \Xi = [-1, 1] \times [0, 1]$ ;  $\nu$  is the viscosity of the system, which is taken as  $(0.01/\pi)$ . The initial and boundary conditions of the above equation are given by

$$u(t = 0, x) = -\sin(\pi x); \quad u(t, x = \pm 1) = 0 \quad (27)$$

With the above equation, a function  $f(t, x)$  is constructed which provides the physical information

of the neural network. It is expressed as follows:

$$f(t, x) = \frac{\partial u}{\partial t} + u \frac{\partial u}{\partial x} - \nu \frac{\partial^2 u}{\partial x^2} \quad (28)$$

The optimal parameters of the neural network are estimated by minimizing the loss function, which is given by

$$\mathcal{L} = \mathcal{L}_u + \mathcal{L}_f \quad (29)$$

where  $\mathcal{L}_u$  denotes mean square error loss, which is calculated using the data corresponding to the initial and boundary conditions, whereas  $\mathcal{L}_f$  denotes the loss corresponding to the function  $f(t, x)$ , defined in Eq. 28. These two loss functions are expressed in the following forms

$$\mathcal{L}_u = \frac{1}{N_u} \sum_{i=1}^{N_u} |u(t_u^i, x_u^i) - u^i|^2 \quad (30a)$$

$$\mathcal{L}_f = \frac{1}{N_f} \sum_{i=1}^{N_f} |f(t_f^i, x_f^i)|^2 \quad (30b)$$

In Eq. 30,  $\{t_u^i, x_u^i, u^i\}$  denotes the initial and boundary training data of the function  $u(t, x)$  where  $N_u$  is the total number of training data. Similarly,  $\{t_f^i, x_f^i\}$  is the training data of the spatio-temporal domain where  $N_f$  is the total number of training data to train  $f(t, x)$ .

In this problem, eight hidden layers, each with 20 neurons are used construct the neural network.

The MSE values for various sizes of DoE sets are shown in Fig. 16. From Fig. 16, it is clear that 400 samples are needed to stabilize the MSE values.

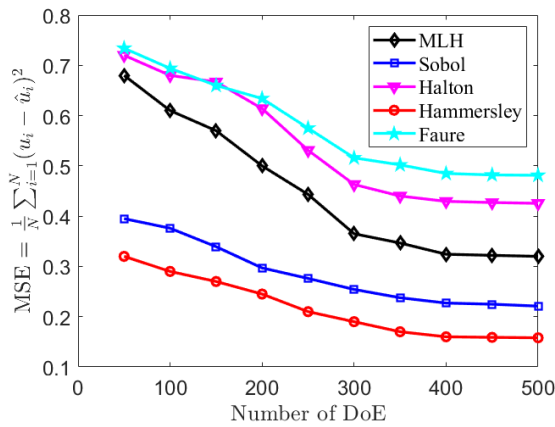


**Fig. 16** The MSE history for different levels of DoE for solving Viscous Burger's equation

With this, a comparative study is performed with all DoE schemes and the absolute errors between actual and predicted responses are shown using a Box and Whisker plot as shown in Fig. 17. In Fig. 17, the red line represents the median value of the errors. By comparing the median values, it can be concluded that FD, CCD, and CVT perform the worst over-fitting. Among those, Hammersley performs best due to a lower median value. SGD and Sobol sampling yield the next best results. Once the accuracy is established, the predicted responses are evaluated considering the 400 DoE samples generated using Hammersley sampling. The contour plots of the actual solution ( $u(t, x)$ ) and predicted solution ( $\hat{u}(t, x)$ ) of the viscous Burger's equation are shown in Fig. 18(a) and Fig. 18(b). The error between these two solutions is shown in Fig. 18(c).

## 4.2 Problem 2 : Shrödinger Equation

Here, the Shrödinger equation is considered as our next example, which is a classical field equation, applied in quantum mechanical systems, nonlinear wave propagation in optical fibres, etc. The nonlinear Shrödinger equation subjected to periodic

boundary conditions is written as [135]:

$$i \frac{\partial u}{\partial t} + \frac{1}{2} \frac{\partial^2 u}{\partial x^2} + u^2 u = 0$$

$$u(0, x) = 2 \operatorname{sech}(x); \quad u(t, -5) = u(t, 5) \quad (31)$$

$$\frac{\partial u}{\partial x}(t, -5) = \frac{\partial u}{\partial x}(t, 5)$$

where  $(x, t) \in \Xi = [-5, 5] \times [0, \pi/2]$ . In the above equation,  $u(x, t)$  is a complex-valued function. A loss function is considered, which has to be minimized to estimate the parameters related to neural networks, is given by

$$\mathcal{L} = \mathcal{L}_0 + \mathcal{L}_b + \mathcal{L}_f \quad (32)$$

where  $\mathcal{L}_0$ ,  $\mathcal{L}_b$ , and  $\mathcal{L}_f$  are the residual loss functions on the initial data, the periodic boundary condition and Shrödinger equation, are written as

$$\mathcal{L}_0 = \frac{1}{N_0} \sum_{j=1}^{N_0} \left| u(0, x_0^j) - u_0^j \right|^2 \quad (33a)$$

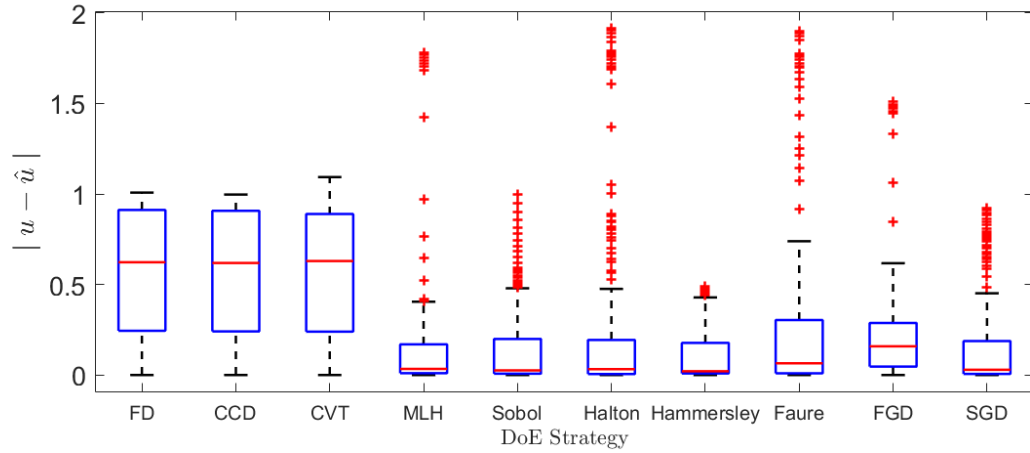
$$\mathcal{L}_b = \frac{1}{N_b} \sum_{j=1}^{N_b} \left\{ \left| u^j(t_b^j, -5) - u^j(t_b^j, 5) \right|^2 + \left| u_x^j(t_b^j, -5) - u_x^j(t_b^j, 5) \right|^2 \right\} \quad (33b)$$

$$\mathcal{L}_f = \frac{1}{N_f} \sum_{j=1}^{N_f} \left| f(t_f^j, x_f^j) \right|^2 \quad (33c)$$

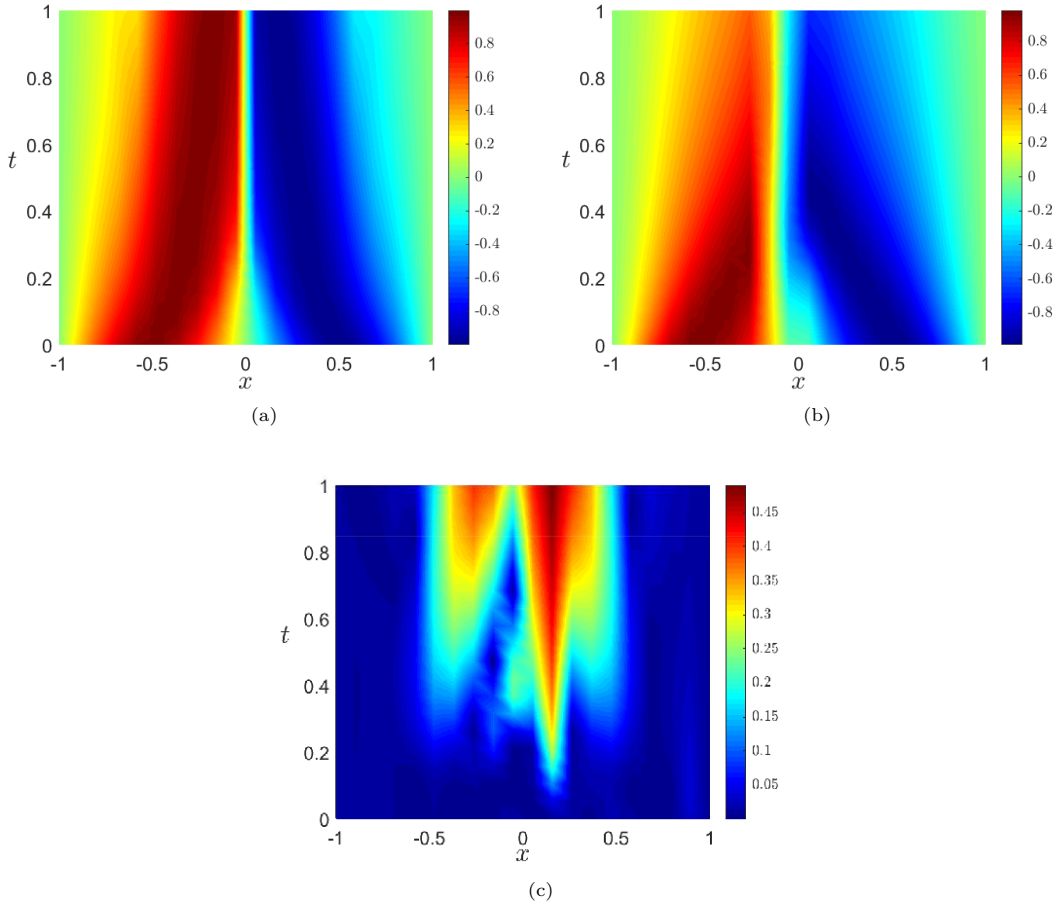
In Eq. 33b,  $u_x$  denotes the first partial derivative of  $u$  with respect to  $x$ , i.e.,  $\partial u / \partial x$ . Also, in Eq. 33c,  $f$  is the function representing Shrödinger equation, as in Eq. 31 i.e.,  $f = iu_t + 0.5u_{xx} + u^2 u$ .

Fig. 19 depicts the MSE values for various DoE set sizes. It is seen that 400 samples are needed to stabilize the MSE values. With this, a comparative study is performed with all DoE schemes and the absolute errors between actual and predicted responses are shown using Box and Whisker plot as shown in Fig. 20. It is seen that FD, CCD and CVT perform the worst by comparing the median values. Apart from FGD, the other DoE strategies such as MLH, SGD, Sobol, Halton, Hammersley, and Faure sampling almost perform the same. Among those, Hammersley sampling slightly performs better. Once the accuracy is established, the predicted responses are evaluated considering the 400 DoE samples generated using

## State-of-the-Art Review of Design of Experiments for PINN



**Fig. 17** Absolute error between original and predicted responses of viscous Burger's equation considering different DoE strategies



**Fig. 18** Viscous Burger's equation: (a) Exact solution; (b) Solution using PINN and (c) Absolute error between exact solution and solution using PINN

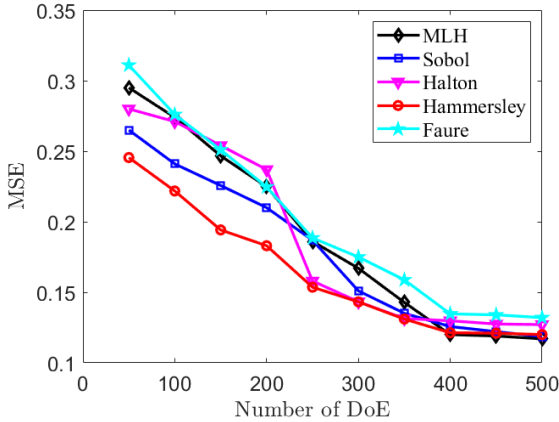


**Fig. 19** The MSE values for different number of DoE sets for different DoE techniques for Shrödinger equation

Hammersley sampling. Fig. 21(a) and Fig. 21(b) show the contour plot of predicted solution of the Shrödinger equation and the error between exact and predicted solutions, respectively.

### 4.3 Problem 3: 1D - Heat Equation

As an example, consider the one-dimensional heat equation, which is a second-order PDE that describes heat diffusion through a material and is written as

$$\frac{\partial u}{\partial t} = \frac{\partial^2 u}{\partial x^2} \quad (34)$$

where  $(x, t) \in \Xi = [0, L] \times [0, 1]$ . Initially, the temperature is a nonzero constant. Therefore, the initial condition is given by

$$u(x, 0) = T_0 \quad (35)$$

Also, the boundary conditions imposed on the system, which are zero at the left boundary and nonzero at the right boundary, is shown in Fig. 22. The boundary conditions are expressed as

$$u(0, t) = 0 \quad u(L, t) = 1 \quad (36)$$

In this study, the parameters  $L$  and  $T_0$  are taken as 1 and 0.5, respectively. The optimal neural network parameters are estimated by minimizing the loss function  $\mathcal{L} = \mathcal{L}_u + \mathcal{L}_f$ . The two components of the loss function are given by

$$\mathcal{L}_u = \frac{1}{N_u} \sum_{i=1}^{N_u} \left| u(t_u^i, x_u^i) - u^i \right|^2 \quad (37a)$$

$$\mathcal{L}_f = \frac{1}{N_f} \sum_{i=1}^{N_f} \left| f(t_f^i, x_f^i) \right|^2 \quad (37b)$$

The loss function corresponding to the initial and boundary conditions is denoted by  $\mathcal{L}_u$ , and the loss function corresponding to the function  $f(t, x)$ , which is defined as  $f = (u_t - u_{xx})$ , is denoted by  $\mathcal{L}_f$ . The network contains eight hidden layers, each with 20 neurons. The MSE values for various sizes of DoE sets are shown in Fig. 23. It is seen that 400 samples are needed to stabilize the MSE values. With this, a comparative study is performed with all DoE schemes and the absolute errors between actual and predicted responses are shown using a Box and Whisker plot as shown in Fig. 24. It is seen that FD and CVT perform the worst by comparing the median values. Among others, Hammersley sampling performs better as its median value is the lowest. Once the accuracy is established, the predicted responses are evaluated considering the 400 DoE samples generated using Hammersley sampling. Fig. 25(a) and Fig. 25(b) show the contour plot of the predicted solution of the one-dimensional heat conduction equation and the error between exact and predicted solutions, respectively.

### 4.4 Problem 4: Allen - Cahn Equation

Allen - Cahn equation, a second - order PDE, is used to represent the physical problems such as crystal growth [136], image segmentation [137], motion by mean curvature flows [138] etc. Mainly, this equation is used to study phase transitions and interfacial dynamics in material science [139]. The governing differential equation is given as

$$\frac{\partial u}{\partial t} - 0.0001 \frac{\partial^2 u}{\partial x^2} + 5u^3 - 5u = 0 \quad (38)$$

where  $(x, t) \in \Xi = [-1, 1] \times [0, 1]$ . The initial and boundary conditions of the above equation are given by

$$\begin{aligned} u(t = 0, x) &= x^3 \cos(\pi x) \\ u(t, x = -1) &= u(t, x = 1) \\ \frac{\partial u}{\partial x}(t, x = -1) &= \frac{\partial u}{\partial x}(t, x = 1) \end{aligned} \quad (39)$$

The parameters related to the neural networks are estimated by minimizing a loss function, which is

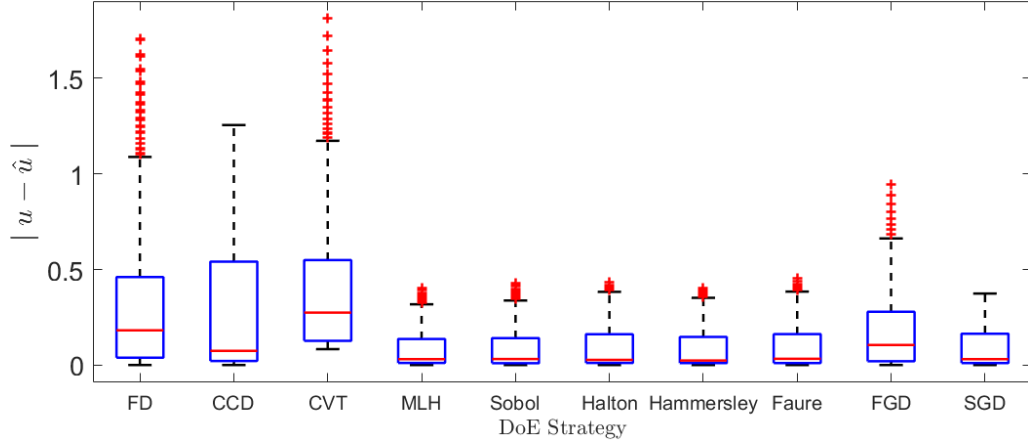


**Fig. 20** Absolute error between original and predicted responses of Shrödinger equation considering different DoE strategies

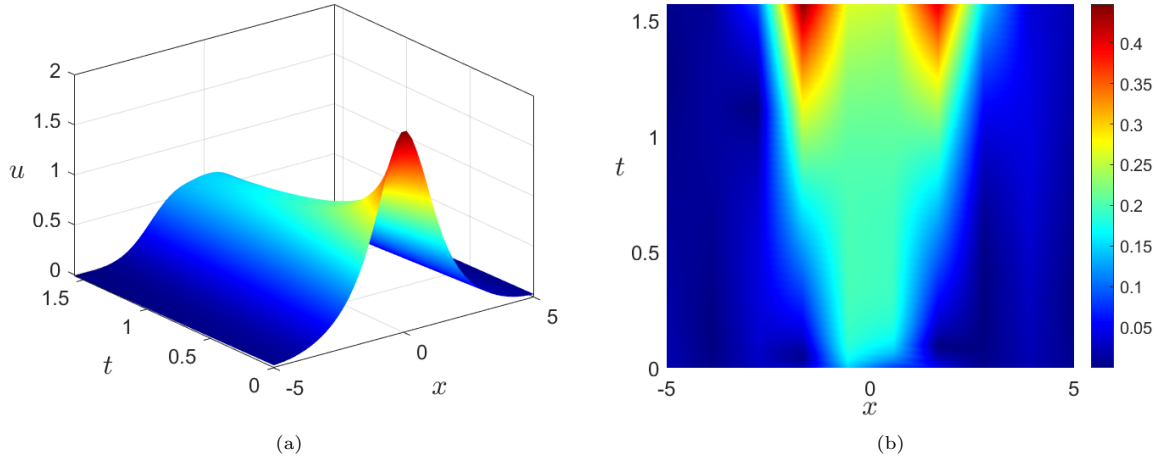


**Fig. 21** Shrödinger equation: (a) Solution for  $u$  using PINN and (b) Absolute error between exact solution and solution using PINN

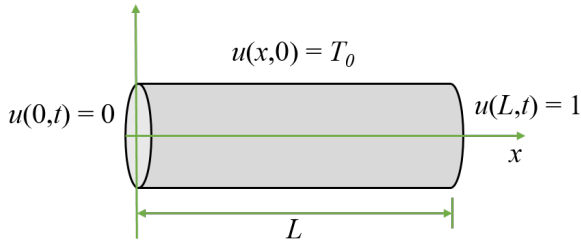


**Fig. 22** Heat conduction in a rod

expressed in the following form

$$\mathcal{L} = \mathcal{L}_0 + \mathcal{L}_b + \mathcal{L}_f \quad (40)$$

where  $\mathcal{L}_0$ ,  $\mathcal{L}_b$ ,  $\mathcal{L}_f$  are the residual loss functions on the initial data, the periodic boundary condition and Allen-Cahn equation, are as follows

$$\mathcal{L}_0 = \frac{1}{N_0} \sum_{j=1}^{N_0} |u(0, x_0^j) - u_0^j|^2 \quad (41a)$$

$$\mathcal{L}_b = \frac{1}{N_b} \sum_{j=1}^{N_b} \left\{ |u^j(t_b^j, -1) - u^j(t_b^j, 1)|^2 + |u_x^j(t_b^j, -1) - u_x^j(t_b^j, 1)|^2 \right\} \quad (41b)$$



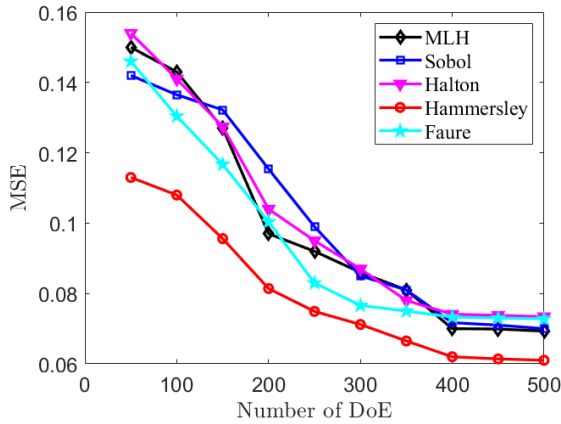


**Fig. 23** The MSE values for different number of DoE sets for different DoE techniques for heat equation

$$\mathcal{L}_f = \frac{1}{N_f} \sum_{j=1}^{N_f} \left| f(t_f^j, x_f^j) \right|^2 \quad (41c)$$

In Eq. 41c,  $f$  represents the Allen-Cahn equation, which is defined in Eq. 38, i.e.,  $f = u_t - 0.0001u_{xx} + 5u^3 - 5u$ . To solve the second-order PDE representing the Allen-Cahn equation, a neural network is designed which contains four hidden layers, each with 200 neurons. The MSE values for various sizes of DoE sets are shown in Fig. 26. It is seen that 400 samples are needed to stabilize the MSE values. Once the size of the DoE set is fixed for quasi-random sampling schemes, a comparative study is performed with all DoE schemes and the absolute errors between actual and predicted responses are shown using the Box and Whisker plot as shown in Fig. 27. It is seen that Hammersley sampling performs better as its maximum value of absolute error is the lowest compared to others. Once the accuracy is established, the predicted responses are evaluated considering the 400 DoE samples generated using Hammersley sampling. Fig. 28(a) and Fig. 28(b) show the contour plot of the predicted solution of the Allen-Cahn equation and the error between exact and predicted solutions, respectively.

#### 4.5 Problem 5: Korteweg-de Vries Equation

As the final example of this study, the Korteweg-de Vries (KdV) equation is considered, which is a nonlinear PDE comprising the higher order derivatives. This equation is used to describe the

small amplitude shallow-water waves, ion-phonon waves, and fluctuation phenomena in biological systems, etc. [140, 141]. The governing KdV equation for shallow-water waves is expressed as

$$\frac{\partial u}{\partial t} + u \frac{\partial u}{\partial x} + \frac{\partial^3 u}{\partial x^3} = 0 \quad (42)$$

where  $(x, t) \in \Xi = [0, 2\pi] \times [0, 1]$ . With the above equation, periodic boundary conditions, i.e.,  $u(t, x = 0) = u(t, x = 2\pi)$  are considered. The initial condition of the KdV equation is given by

$$u(t = 0, x) = A \operatorname{sech}^2 \left( \sqrt{\frac{A}{12}} (x - \pi) \right) \quad (43)$$

The optimal neural network parameters are determined by minimizing the loss functions ( $\mathcal{L} = \mathcal{L}_u + \mathcal{L}_f$ ), which are written as follows

$$\mathcal{L}_u = \frac{1}{N_u} \sum_{i=1}^{N_u} \left| u(t_u^i, x_u^i) - u^i \right|^2 \quad (44a)$$

$$\mathcal{L}_f = \frac{1}{N_f} \sum_{i=1}^{N_f} \left| f(t_f^i, x_f^i) \right|^2 \quad (44b)$$

where  $\mathcal{L}_u$  and  $\mathcal{L}_f$  are the loss functions corresponding to the initial and boundary conditions, and the function  $f(t, x)$ , defined in Eq. 42. The function  $f$  in Eq. 44 represents the KdV equation, defined in Eq. 42, i.e.,  $f = u_t + uu_x + u_{xxx}$ . To solve the higher-order PDE representing the KdV equation, a neural network is designed which contains seven hidden layers, each with 120 neurons. The MSE values for various sizes of DoE sets are shown in Fig. 29. It is seen that 350 samples are needed to stabilize the MSE values.

Once the size of the DoE set is fixed for quasi-random sampling schemes, a comparative study is performed with all DoE schemes and the absolute errors between actual and predicted responses are shown using the Box and Whisker plot as shown in Fig. 30. It is seen that Hammersley sampling performs better. Once the accuracy is established, the predicted responses are evaluated considering the 350 DoE samples generated using Hammersley sampling. Fig. 31(a) and Fig. 31(b) show the contour plot of the predicted solution of the KdV equation and the error between exact and predicted solutions, respectively.

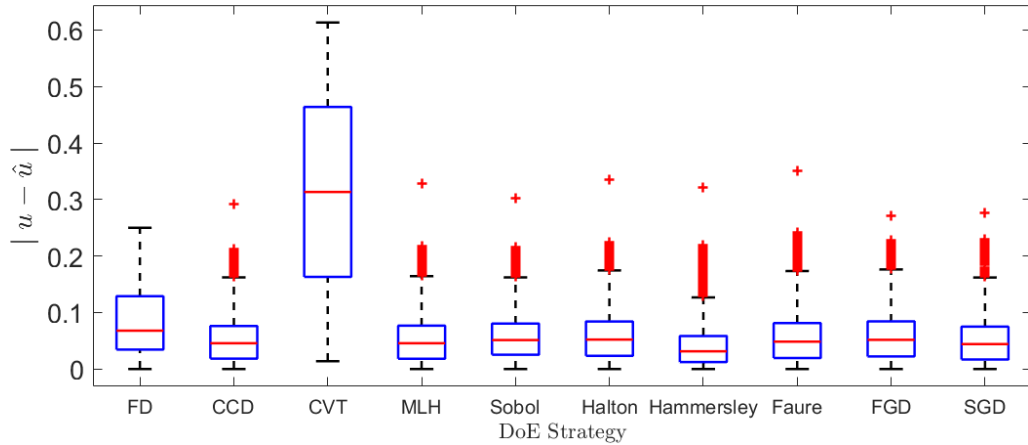


**Fig. 24** Absolute error between original and predicted responses of heat equation considering different DoE strategies

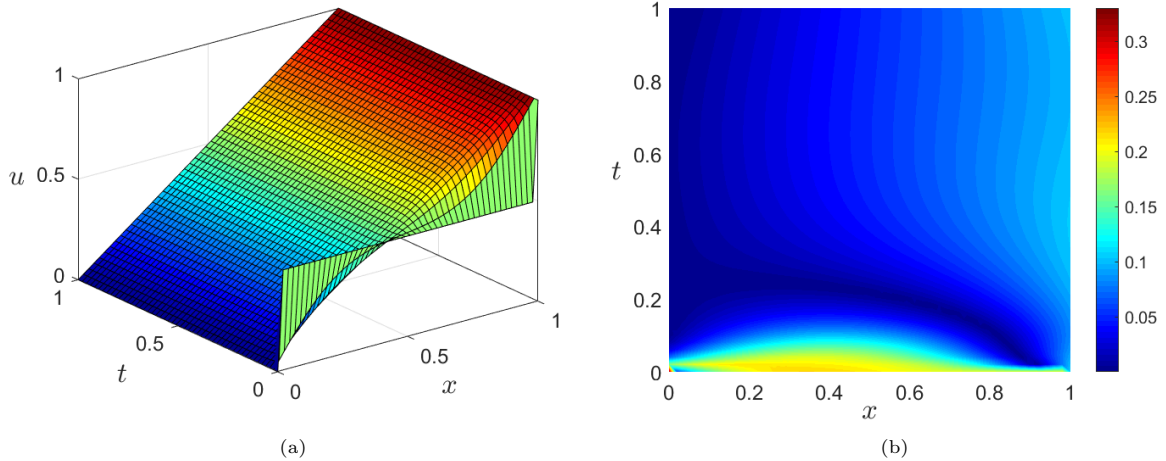


**Fig. 25** (a) Solution for  $u$  using PINN and (b) Absolute error between exact solution and solution using PINN for heat conduction equation

## 5 Conclusion

The selection of the design of experiment strategy plays an important role in predicting the output using surrogate models. The surrogate model predicts the output based on the training data by minimizing the residuals between the output corresponding to the training data and predicted responses. An extensive survey of the different DoE strategies is presented in this study. A review of classical and modern experimental strategy design is also provided. This study is only focused on the physics-informed neural network. In this context, a few salient observations are highlighted below-

- Here, five different partial differential equations i.e., Viscous Burger's equation, Schrödinger equation, one-dimensional heat equation, Allen-Cahn equation and Korteweg-de Vries equation are considered for investigation purposes. To solve these equations, a physics-based deep neural network method is used, which is trained using the training data generated by different DoE schemes. It is seen that quasi-random sampling techniques, especially the Hammersley sampling scheme, yield better results compared to classical DoE schemes. This argument is established based on comparing the absolute error between the actual and predicted

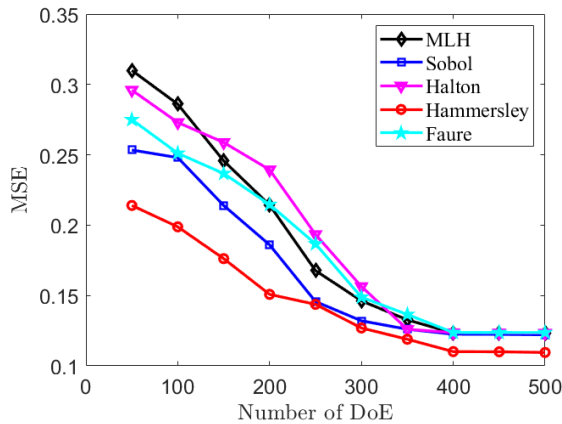


**Fig. 26** The MSE values for different number of DoE sets for different DoE techniques for Allen-Cahn equation

solutions. This reflects that the Hammersley sampling covers the whole design space better than other DoE strategies.

- The size of the DoE set affects the accuracy of the surrogate model. For high-fidelity models where the computational budget is expensive, the smallest size of the training set is needed to estimate to reduce the computational budget as well as the accuracy of the prediction. In this study, it is seen that at least 350 to 400 DoE samples are taken to get accurate predicted responses.

In general, this paper emphasises the importance of choosing a DoE scheme in order to obtain accurate predicted responses using a physics-informed neural network. In this context, it may be noted that the present study does not consider any sequential method where one sample is added to the DoE set used in the previous iteration based on some performance measures.

## Acknowledgments

This study was funded by Natural Sciences and Engineering Research Council of Canada under the Discovery Grant programs (RGPIN-2019-05584). Development of the design guideline in this study was supported through the BC Forestry Innovation Investment's (FII) Wood First Program.

## Conflict of interest

The authors declare that they have no known competing financial interests or personal relationships that could have appeared to influence the work reported in this paper.

## References

- [1] Der Kiureghian, A., Ditlevsen, O.: Aleatory or epistemic? Does it matter? *Structural Safety* **31**(2), 105–112 (2009)
- [2] Sheppard, C.: Computer simulation of stochastic processes through model-sampling (Monte Carlo) techniques. *FEBS letters* **2**, 14–21 (1969)
- [3] Montgomery, D.C.: *Design and Analysis of Experiments*. John Wiley & Sons (2017)
- [4] Rathi, A.K., Sharma, P.V.S., Chakraborty, A.: Sequential Stochastic Response Surface Method Using Moving Least Squares-Based Sparse Grid Scheme for Efficient Reliability Analysis. *International Journal of Computational Methods* **16**(05), 1840017 (2019)
- [5] Xiu, D., Karniadakis, G.E.: The Wiener–Askey polynomial chaos for stochastic differential equations. *SIAM Journal on Scientific Computing* **24**(2), 619–644 (2002)
- [6] Sudret, B.: Global sensitivity analysis using polynomial chaos expansions. *Reliability Engineering & System Safety* **93**(7), 964–979 (2008)
- [7] Matheron, G.: Kriging or polynomial interpolation procedures. *CIMM Transactions* **70**, 240–244 (1967)
- [8] Das, S., Tesfamariam, S.: Optimization of SMA based damped outrigger structure under uncertainty. *Engineering Structures* **222**, 111074 (2020)
- [9] Schobi, R., Sudret, B., Wiart, J.: Polynomial-chaos-based Kriging. *International Journal for Uncertainty Quantification* **5**(2) (2015)

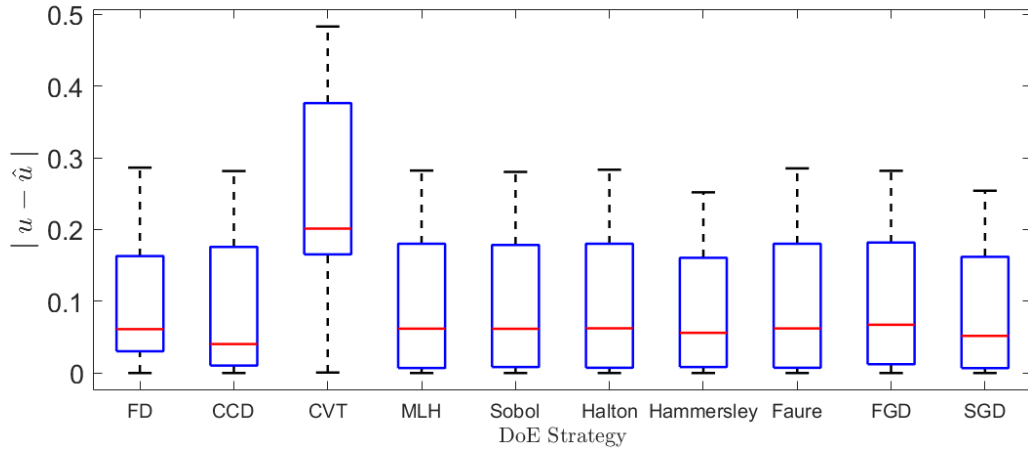


**Fig. 27** Absolute error between original and predicted responses of Allen-Cahn equation considering different DoE strategies

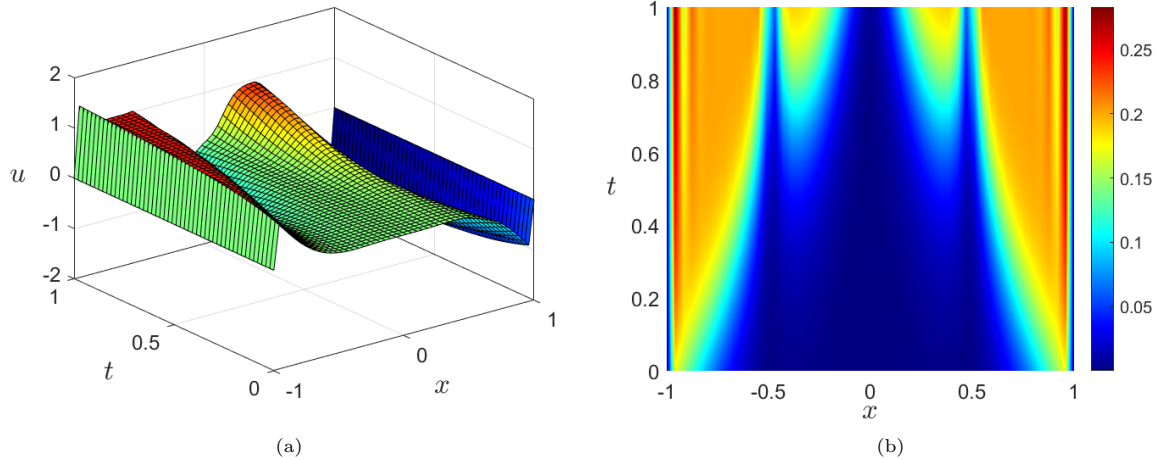


**Fig. 28** (a) Solution for  $u$  using PINN and (b) Absolute error between exact solution and solution using PINN for reaction - diffusion system represented by Allen-Cahn equation

- [10] Rathi, A.K., Chakraborty, A.: Development of hybrid dimension adaptive sparse HDMR for stochastic finite element analysis of composite plate. *Composite Structures* **255**, 112915 (2021)
- [11] Rathi, A.K., Chakraborty, A.: Improved Moving Least Square-Based Multiple Dimension Decomposition (MDD) Technique for Structural Reliability Analysis. *International Journal of Computational Methods* **18**(01), 2050024 (2021)
- [12] Wang, S., Wang, M.Y.: Radial basis functions and level set method for structural topology optimization. *International Journal for Numerical Methods in Engineering* **65**(12), 2060–2090 (2006)
- [13] De Marchi, S., Santin, G.: A new stable basis for radial basis function interpolation. *Journal of Computational and Applied Mathematics* **253**, 1–13 (2013)
- [14] Xiao, M., Gao, L., Xiong, H., Luo, Z.: An efficient method for reliability analysis

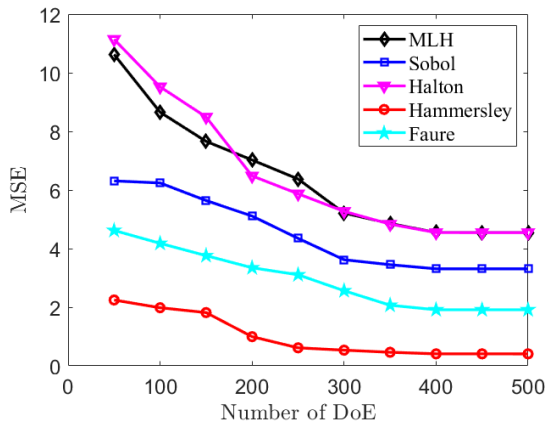


**Fig. 29** The MSE values for different number of DoE sets for different DoE techniques for KdV equation

under epistemic uncertainty based on evidence theory and support vector regression. *Journal of Engineering Design* **26**(10-12), 340–364 (2015)

- [15] Hassoun, M.H., et al.: *Fundamentals of Artificial Neural Networks*. MIT press (1995)
- [16] Das, S., Chakraborty, A., Barua, I.: Optimal tuning of SMA inerter for simultaneous wind induced vibration control of high-rise building and energy harvesting. *Smart Materials and Structures* **30**(2), 025027 (2021)
- [17] Murphy, K.P.: *Machine Learning: a Probabilistic Perspective*. MIT press (2012)
- [18] Mitchell, T.: *Machine Learning*. McGraw-Hill (1997)
- [19] Raissi, M., Karniadakis, G.E.: Hidden physics models: Machine learning of nonlinear partial differential equations. *Journal of Computational Physics* **357**, 125–141 (2018)
- [20] Raissi, M., Yazdani, A., Karniadakis, G.E.: Hidden fluid mechanics: Learning velocity and pressure fields from flow visualizations. *Science* **367**(6481), 1026–1030 (2020)
- [21] Rad, M.T., Viardin, A., Schmitz, G., Apel, M.: Theory-training deep neural networks for an alloy solidification benchmark problem. *Computational Materials Science* **180**, 109687 (2020)
- [22] Shin, Y., Darbon, J., Karniadakis, G.E.: On the convergence and generalization of physics informed neural networks. arXiv e-prints, 2004 (2020)
- [23] Haghghat, E., Raissi, M., Moure, A., Gomez, H., Juanes, R.: A deep learning framework for solution and discovery in solid mechanics: linear elasticity. arXiv preprint arXiv:2003.02751 (2020)
- [24] He, Z., Ni, F., Wang, W., Zhang, J.: A physics-informed deep learning method for solving direct and inverse heat conduction problems of materials. *Materials Today Communications* **28**, 102719 (2021)
- [25] Olivieri, M., Pezzoli, M., Antonacci, F., Sarti, A.: A Physics-Informed Neural Network Approach for Nearfield Acoustic Holography. *Sensors* **21**(23), 7834 (2021)
- [26] Eker, O.F., Camci, F., Jennions, I.K.: A New Hybrid Prognostic Methodology. *International Journal of Prognostics and Health Management* **10**(2) (2019)
- [27] Yucesan, Y.A., Viana, F.A.: A Physics-informed Neural Network for Wind Turbine Main Bearing Fatigue. *International Journal of Prognostics and Health Management* **11**(1) (2020)
- [28] Cheng, C., Meng, H., Li, Y.-Z., Zhang, G.-T.: Deep learning based on PINN for solving 2 DOF vortex induced vibration of cylinder. *Ocean Engineering* **240**, 109932 (2021)
- [29] Bai, X., Zhang, W.: Machine Learning for Vortex Induced Vibration in Turbulent Flow. arXiv preprint arXiv:2103.05818 (2021)
- [30] Sun, L., Gao, H., Pan, S., Wang, J.-X.: Surrogate modeling for fluid flows based on physics-constrained deep learning without simulation data. *Computer Methods in Applied Mechanics and Engineering* **361**, 112732 (2020)

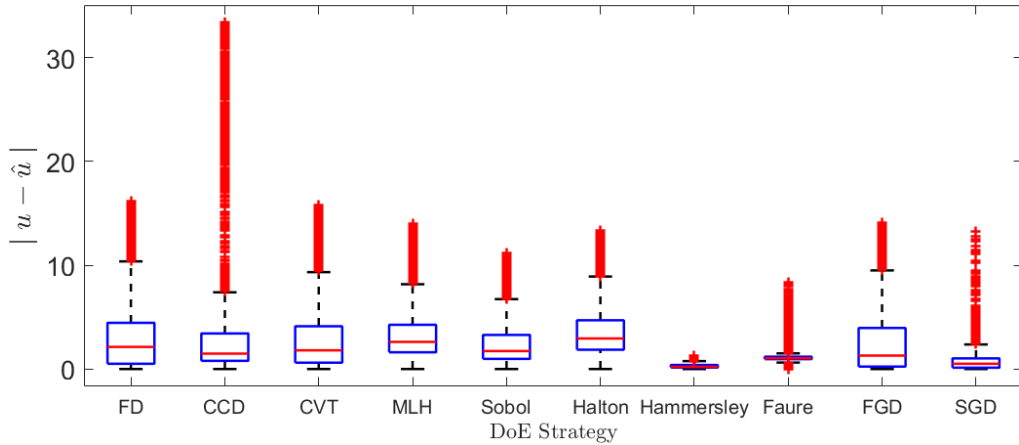


**Fig. 30** Absolute error between original and predicted responses of KdV equation considering different DoE strategies

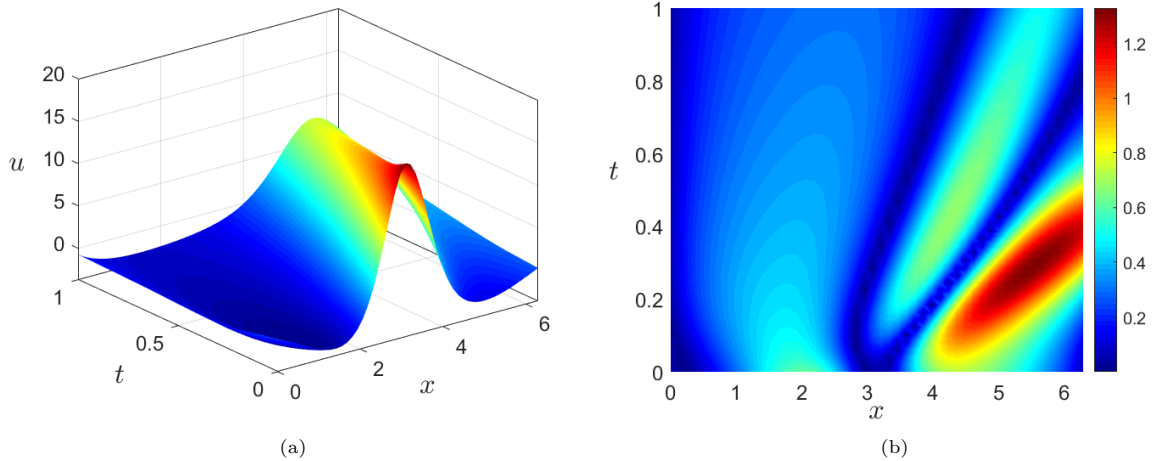


**Fig. 31** (a) Solution for  $u$  using PINN and (b) Absolute error between exact solution and solution using PINN for solitary waves represented by KdV equation

- [31] Tang, H., Yang, H., Liao, Y., Xie, L.: A transfer learning enhanced the physics-informed neural network model for vortex-induced vibration. arXiv preprint arXiv:2112.14448 (2021)
- [32] Song, C., Alkhalifah, T., Waheed, U.B.: A versatile framework to solve the Helmholtz equation using physics-informed neural networks. *Geophysical Journal International* **228**(3), 1750–1762 (2022)
- [33] Karimpouli, S., Tahmasebi, P.: Physics informed machine learning: Seismic wave equation. *Geoscience Frontiers* **11**(6), 1993–2001 (2020)
- [34] Alkhalifah, T., Song, C., Waheed, U.B., Hao, Q.: Wavefield Solutions from Machine Learned Functions that Approximately Satisfy the Wave Equation. In: *EAGE 2020 Annual Conference & Exhibition Online*, vol. 2020, pp. 1–5 (2020). European Association of Geoscientists & Engineers
- [35] Smith, J.D., Azzizadenesheli, K., Ross, Z.E.: EikoNet: Solving the Eikonal Equation With Deep Neural Networks. *IEEE Transactions*

- on Geoscience and Remote Sensing (2020)
- [36] Waheed, U.b., Haghighat, E., Alkhali-fah, T.: Anisotropic eikonal solution using physics-informed neural networks. *Society of Exploration Geophysicists* (2020)
- [37] Patel, R.G., Manickam, I., Trask, N.A., Wood, M.A., Lee, M., Tomas, I., Cyr, E.C.: Thermodynamically consistent physics-informed neural networks for hyperbolic systems. *Journal of Computational Physics* **449**, 110754 (2022)
- [38] Kadeethum, T., Jørgensen, T.M., Nick, H.M.: Physics-informed neural networks for solving nonlinear diffusivity and Biot's equations. *PloS One* **15**(5), 0232683 (2020)
- [39] Lu, L., Pestourie, R., Yao, W., Wang, Z., Verdugo, F., Johnson, S.G.: Physics-informed neural networks with hard constraints for inverse design. *arXiv preprint arXiv:2102.04626* (2021)
- [40] Schiassi, E., De Florio, M., Ganapol, B.D., Picca, P., Furfaro, R.: Physics-informed neural networks for the point kinetics equations for nuclear reactor dynamics. *Annals of Nuclear Energy*, 108833 (2021)
- [41] Dourado, A., Viana, F.A.: Physics-informed neural networks for corrosion-fatigue prognosis. In: *Proceedings of the Annual Conference of the PHM Society*, vol. 11 (2019)
- [42] Penwarden, M., Zhe, S., Narayan, A., Kirby, R.M.: Multifidelity Modeling for Physics-Informed Neural Networks (PINNs). *Journal of Computational Physics*, 110844 (2021)
- [43] Kovacs, A., Exl, L., Kornell, A., Fischbacher, J., Hovorka, M., Gusenbauer, M., Breth, L., Oezelt, H., Praetorius, D., Suess, D., et al.: Magnetostatics and micromagnetics with physics informed neural networks. *Journal of Magnetism and Magnetic Materials*, 168951 (2022)
- [44] Fang, Z., Zhan, J.: Deep physical informed neural networks for metamaterial design. *IEEE Access* **8**, 24506–24513 (2019)
- [45] Kovacs, A., Exl, L., Kornell, A., Fischbacher, J., Hovorka, M., Gusenbauer, M., Breth, L., Oezelt, H., Yano, M., Sakuma, N., et al.: Conditional physics informed neural networks. *Communications in Nonlinear Science and Numerical Simulation* **104**, 106041 (2022)
- [46] Jagtap, A.D., Kharazmi, E., Karniadakis, G.E.: Conservative physics-informed neural networks on discrete domains for conservation laws: Applications to forward and inverse problems. *Computer Methods in Applied Mechanics and Engineering* **365**, 113028 (2020)
- [47] Kharazmi, E., Zhang, Z., Karniadakis, G.E.: Variational physics-informed neural networks for solving partial differential equations. *arXiv preprint arXiv:1912.00873* (2019)
- [48] Meng, X., Li, Z., Zhang, D., Karniadakis, G.E.: PPINN: Parareal physics-informed neural network for time-dependent PDEs. *Computer Methods in Applied Mechanics and Engineering* **370**, 113250 (2020)
- [49] O'Leary, J., Paulson, J.A., Mesbah, A.: Stochastic Physics-Informed Neural Networks (SPINN): A Moment-Matching Framework for Learning Hidden Physics within Stochastic Differential Equations. *arXiv preprint arXiv:2109.01621* (2021)
- [50] Pang, G., Lu, L., Karniadakis, G.E.: fPINNs: Fractional Physics-Informed Neural Networks. *SIAM Journal on Scientific Computing* **41**(4), 2603–2626 (2019)
- [51] Pang, G., D'Elia, M., Parks, M., Karniadakis, G.E.: nPINNs: nonlocal Physics-Informed Neural Networks for a parametrized nonlocal universal Laplacian operator. *Algorithms and Applications. Journal of Computational Physics* **422**, 109760 (2020)
- [52] Jagtap, A.D., Karniadakis, G.E.:

*State-of-the-Art Review of Design of Experiments for PINN*

- Extended physics-informed neural networks (XPINNs): A generalized space-time domain decomposition based deep learning framework for nonlinear partial differential equations. *Communications in Computational Physics* **28**(5), 2002–2041 (2020)
- [53] Shukla, K., Jagtap, A.D., Karniadakis, G.E.: Parallel physics-informed neural networks via domain decomposition. *Journal of Computational Physics* **447**, 110683 (2021)
- [54] Kharazmi, E., Zhang, Z., Karniadakis, G.E.: hp-VPINNs: Variational physics-informed neural networks with domain decomposition. *Computer Methods in Applied Mechanics and Engineering* **374**, 113547 (2021)
- [55] Fisher, R.A.: The arrangement of field experiments. *Ministry of Agriculture* **33**, 503–513 (1926)
- [56] Koehler, J.R., Owen, A.B.: Computer experiments. *Handbook of Statistics* **13**, 261–308 (1996)
- [57] Santner, T.J., Williams, B.J., Notz, W.I., Williams, B.J.: *The Design and Analysis of Computer Experiments*. Springer (2003)
- [58] Anderson, V.L., McLean, R.A.: *Design of Experiments: A Realistic Approach*. Marcel Dekker Inc., New York (1974)
- [59] Lorenzen, T., Anderson, V.: *Design of Experiments: A No-Name Approach*. CRC Press (1993)
- [60] Mason, R.L., Gunst, R.F., Hess, J.L.: *Statistical Design and Analysis of Experiments With Applications to Engineering and Science*. John Wiley & Sons (2003)
- [61] Antony, J.: *Design of Experiments for Engineers and Scientists*. Elsevier (2014)
- [62] Sacks, J., Schiller, S.B., Welch, W.J.: Designs for Computer Experiments. *Technometrics* **31**(1), 41–47 (1989)
- [63] Chen, V.C., Tsui, K.-L., Barton, R.R., Allen, J.K.: A review of design and modeling in computer experiments. *Handbook in Statistics: Statistics in Industry* (2002)
- [64] Crary, S.B.: *Design of Computer Experiments for Metamodel Generation*. *Analog Integrated Circuits and Signal Processing* **32**(1), 7–16 (2002)
- [65] Box, G., Wilson, K.: On the Experimental Attainment of Optimum Conditions. *Journal of the Royal Statistical Society, Series B (Methodological)* **13**(1), 1–45 (1951)
- [66] Ferreira, S.C., Bruns, R., Ferreira, H., Matos, G., David, J., Brandão, G., da Silva, E.P., Portugal, L., Dos Reis, P., Souza, A., *et al.*: Box-Behnken design: An alternative for the optimization of analytical methods. *Analytica Chimica Acta* **597**(2), 179–186 (2007)
- [67] Kiefer, J., Wolfowitz, J.: Optimum Designs in Regression Problems. *The annals of mathematical statistics*, 271–294 (1959)
- [68] Helton, J.C., Davis, F.J.: Latin hypercube sampling and the propagation of uncertainty in analyses of complex systems. *Reliability Engineering & System Safety* **81**(1), 23–69 (2003)
- [69] Hedayat, A.S., Sloane, N.J.A., Stufken, J.: *Orthogonal Arrays: Theory and Applications*. Springer (1999)
- [70] Li, R.: Model selection for analysis of uniform design and computer experiment. *International Journal of Reliability, Quality and Safety Engineering* **9**(04), 367–382 (2002)
- [71] Kroese, D.P., Taimre, T., Botev, Z.I.: *Handbook of Monte Carlo Methods*. John Wiley & Sons (2013)
- [72] Gelfand, A.E.: Gibbs sampling. *Journal of the American statistical Association* **95**(452), 1300–1304 (2000)
- [73] Chib, S., Greenberg, E.: Understanding the



- Metropolis-Hastings Algorithm. The American Statistician **49**(4), 327–335 (1995)
- [74] Du, Q., Faber, V., Gunzburger, M.: Centroidal Voronoi Tessellations: Applications and Algorithms. *SIAM Review* **41**(4), 637–676 (1999)
- [75] Johnson, M.E., Moore, L.M., Ylvisaker, D.: Minimax and maximin distance designs. *Journal of statistical planning and inference* **26**(2), 131–148 (1990)
- [76] Sobol', I.M.: On the distribution of points in a cube and the approximate evaluation of integrals. *USSR Computational Mathematics and Mathematical Physics* **7**(4), 86–112 (1967)
- [77] Halton, J.H.: On the efficiency of certain quasi-random sequences of points in evaluating multi-dimensional integrals. *Numerische Mathematik* **2**(1), 84–90 (1960)
- [78] Wong, T.-T., Luk, W.-S., Heng, P.-A.: Sampling with hammersley and halton points. *Journal of Graphics Tools* **2**(2), 9–24 (1997)
- [79] Faure, H.: Discrépance de suites associées à un système de numération (en dimension  $s$ ). *Acta arithmetica* **41**(4), 337–351 (1982)
- [80] Doehlert, D.H.: Uniform Shell Designs. *Journal of the Royal Statistical Society: Series C (Applied Statistics)* **19**(3), 231–239 (1970)
- [81] Hibbert, D.B.: Experimental design in chromatography: A tutorial review. *Journal of Chromatography B* **910**, 2–13 (2012)
- [82] Bezerra, M.A., Santelli, R.E., Oliveira, E.P., Villar, L.S., Escalera, L.A.: Response surface methodology (RSM) as a tool for optimization in analytical chemistry. *Talanta* **76**(5), 965–977 (2008)
- [83] Elfving, G.: Optimum Allocation in Linear Regression Theory. *The Annals of Mathematical Statistics*, 255–262 (1952)
- [84] Kiefer, J.: Optimum experimental designs V, with applications to systematic and rotatable designs. In: *Proceedings of the Fourth Berkeley Symposium on Mathematical Statistics and Probability, Volume 1: Contributions to the Theory of Statistics*, pp. 381–405 (1961). University of California Press
- [85] Bondar, J.V.: Universal optimality of experimental designs: definitions and a criterion. *Canadian Journal of Statistics* **11**(4), 325–331 (1983)
- [86] Breiman, L.: Discussion: Multivariate Adaptive Regression Splines. *The Annals of Statistics* **19**(1), 82–91 (1991)
- [87] Pukelsheim, F.: *Optimal Design of Experiments*. Inc., New York, New York (1993)
- [88] Parkinson, A., Sorensen, C., Pourhassan, N.: A General Approach for Robust Optimal Design. *Journal of Mechanical Design* **115**(1), 74–80 (1993)
- [89] Jin, R., Chen, W., Sudjianto, A.: An efficient algorithm for constructing optimal design of computer experiments. *Journal of Statistical Planning and Inference* **134**(1), 268–287 (2005)
- [90] Taguchi, G.: Linear graphs for orthogonal arrays and their applications to experimental designs, with the aid of various techniques. Report of Statistical Applications Research, Japanese Union of Scientists and Engineers **6**, 1–43 (1959)
- [91] Kacker, R.N., Lagergren, E.S., Filliben, J.J.: Taguchi's Orthogonal Arrays Are Classical Designs of Experiments. *Journal of research of the National Institute of Standards and Technology* **96**(5), 577 (1991)
- [92] Owen, A.B.: Orthogonal arrays for computer experiments, integration and visualization. *Statistica Sinica*, 439–452 (1992)
- [93] Gentle, J.E.: *Random Number Generation and Monte Carlo Methods*. Springer (2003)
- [94] Fang, K.-T., Li, R., Sudjianto, A.: *Design*

*State-of-the-Art Review of Design of Experiments for PINN*

and Modeling for Computer Experiments. Chapman and Hall/CRC (2005)

- [95] Liu, J.S., Liu, J.S.: Monte Carlo Strategies in Scientific Computing. Springer (2001)
- [96] Robert, C.P., Casella, G., Casella, G.: Monte Carlo Statistical Methods. Springer (2004)
- [97] Romero, V.J., Burkardt, J.V., Gunzburger, M.D., Peterson, J.S.: Comparison of pure and “Latinized” centroidal Voronoi tessellation against various other statistical sampling methods. *Reliability Engineering & System Safety* **91**(10-11), 1266–1280 (2006)
- [98] Stein, M.: Large Sample Properties of Simulations Using Latin Hypercube Sampling. *Technometrics* **29**(2), 143–151 (1987)
- [99] Chen, R.-B., Hsieh, D.-N., Hung, Y., Wang, W.: Optimizing Latin hypercube designs by particle swarm. *Statistics and Computing* **23**(5), 663–676 (2013)
- [100] Viana, F.A.: A Tutorial on Latin Hypercube Design of Experiments. *Quality and Reliability Engineering International* **32**(5), 1975–1985 (2016)
- [101] Bratley, P., Fox, B.L.: Algorithm 659: Implementing Sobol’s quasirandom sequence generator. *ACM Transactions on Mathematical Software (TOMS)* **14**(1), 88–100 (1988)
- [102] Owen, A.B.: Scrambling Sobol’ and Niederreiter–Xing Points. *Journal of Complexity* **14**(4), 466–489 (1998)
- [103] Sobol’, I.M., Asotsky, D., Kreinin, A., Kucherenko, S.: Construction and Comparison of High-Dimensional Sobol’ Generators. *Wilmott* **2011**(56), 64–79 (2011)
- [104] Chi, H., Mascagni, M., Warnock, T.: On the optimal Halton sequence. *Mathematics and Computers in Simulation* **70**(1), 9–21 (2005)
- [105] Weerasinghe, G., Chi, H., Cao, Y.: Particle Swarm Optimization Simulation via Optimal Halton Sequences. *Procedia Computer Science* **80**, 772–781 (2016)
- [106] Hokayem, P.F., Abdallah, C.T.: Quasi-Monte Carlo Methods in Robust Control Design. In: 42nd IEEE International Conference on Decision and Control (IEEE Cat. No. 03CH37475), vol. 3, pp. 2435–2440 (2003). IEEE
- [107] Dai, H., Wang, W.: Application of low-discrepancy sampling method in structural reliability analysis. *Structural Safety* **31**(1), 55–64 (2009)
- [108] Ju, L., Du, Q., Gunzburger, M.: Probabilistic methods for centroidal Voronoi tessellations and their parallel implementations. *Parallel Computing* **28**(10), 1477–1500 (2002)
- [109] Kamath, C.: Intelligent Sampling for Surrogate Modeling, Hyperparameter Optimization, and Data Analysis. Technical report, Lawrence Livermore National Lab.(LLNL), Livermore, CA (United States) (2021)
- [110] Tatang, M.A.: Direct incorporation of uncertainty in chemical and environmental engineering systems. PhD thesis, Massachusetts Institute of Technology (1996)
- [111] Mathelin, L., Hussaini, M.Y., Zang, T.A.: Stochastic Approaches to Uncertainty Quantification in CFD Simulations. *Numerical Algorithms* **38**(1-3), 209–236 (2005)
- [112] Xiu, D., Hesthaven, J.S.: High-Order Collocation Methods for Differential Equations with Random Inputs. *SIAM Journal on Scientific Computing* **27**(3), 1118–1139 (2005)
- [113] Holtz, M.: Sparse Grid Quadrature in High Dimensions with Applications in Finance and Insurance. Springer (2010)
- [114] Klimke, A., Wohlmuth, B.: Computing expensive multivariate functions of fuzzy numbers using sparse grids. *Fuzzy Sets and Systems* **154**(3), 432–453 (2005)
- [115] Bungartz, H.-J., Griebel, M.: Sparse grids.

- Acta Numerica **13**(1), 147–269 (2004)
- [116] Barthelmann, V., Novak, E., Ritter, K.: High dimensional polynomial interpolation on sparse grids. *Advances in Computational Mathematics* **12**(4), 273–288 (2000)
- [117] Wu, J., Zhang, D., Jiang, C., Han, X., Li, Q.: On reliability analysis method through rotational sparse grid nodes. *Mechanical Systems and Signal Processing* **147**, 107106 (2021)
- [118] Burkov, A.: *The Hundred-Page Machine Learning Book*. Andriy Burkov Canada (2019)
- [119] Gomes, G.S.d.S., Ludermir, T.B.: Optimization of the weights and asymmetric activation function family of neural network for time series forecasting. *Expert Systems with Applications* **40**(16), 6438–6446 (2013)
- [120] Sodhi, S.S., Chandra, P.: Bi-modal derivative activation function for sigmoidal feed-forward networks. *Neurocomputing* **143**, 182–196 (2014)
- [121] Gomes, G.S.d.S., Ludermir, T.B.: Complementary Log-Log and Probit: Activation Functions Implemented in Artificial Neural Networks. In: 2008 Eighth International Conference on Hybrid Intelligent Systems, pp. 939–942 (2008). IEEE
- [122] Gomes, G.S.d.S., Ludermir, T.B., Lima, L.M.: Comparison of new activation functions in neural network for forecasting financial time series. *Neural Computing and Applications* **20**(3), 417–439 (2011)
- [123] Elliott, D.L.: A better Activation Function for Artificial Neural Networks. Technical report (1993)
- [124] Singh, Y., Chandra, P.: A class+ 1 sigmoidal activation functions for FFANNs. *Journal of Economic Dynamics and Control* **28**(1), 183–187 (2003)
- [125] Burhani, H., Feng, W., Hu, G.: Denoising AutoEncoder in Neural Networks with Modified Elliott Activation Function and Sparsity-Favoring Cost Function. In: 2015 3rd International Conference on Applied Computing and Information Technology/2nd International Conference on Computational Science and Intelligence, pp. 343–348 (2015). IEEE
- [126] Duch, W., Jankowski, N.: Survey of Neural Transfer Functions. *Neural Computing Surveys* **2**(1), 163–212 (1999)
- [127] Chandra, P., Singh, Y.: A case for the self-adaptation of activation functions in FFANNs. *Neurocomputing* **56**, 447–454 (2004)
- [128] Yuan, M., Hu, H., Jiang, Y., Hang, S.: A new camera calibration based on neural network with tunable activation function in intelligent space. In: 2013 Sixth International Symposium on Computational Intelligence and Design, vol. 1, pp. 371–374 (2013). IEEE
- [129] Chandra, P., Sodhi, S.S.: A skewed derivative activation function for SFFANNs. In: International Conference on Recent Advances and Innovations in Engineering (ICRAIE-2014), pp. 1–6 (2014). IEEE
- [130] Hara, K., Nakayama, K.: Comparison of activation functions in multilayer neural network for pattern classification. In: Proceedings of 1994 IEEE International Conference on Neural Networks (ICNN'94), vol. 5, pp. 2997–3002 (1994). IEEE
- [131] Abadi, M., Barham, P., Chen, J., Chen, Z., Davis, A., Dean, J., Devin, M., Ghemawat, S., Irving, G., Isard, M., *et al.*: Tensorflow: A system for large-scale machine learning. In: 12th {USENIX} Symposium on Operating Systems Design and Implementation ({OSDI} 16), pp. 265–283 (2016)
- [132] Haghghat, E., Juanes, R.: SciANN: A Keras/TensorFlow wrapper for scientific computations and physics-informed deep learning using artificial neural networks. *Computer Methods in Applied Mechanics and Engineering* **373**, 113552 (2021)

- [133] Dafermos, C.M.: Hyperbolic Conservation Laws in Continuum Physics. Springer (2005)
- [134] Raissi, M.: Deep hidden physics models: Deep learning of nonlinear partial differential equations. *The Journal of Machine Learning Research* **19**(1), 932–955 (2018)
- [135] Raissi, M., Perdikaris, P., Karniadakis, G.E.: Physics-informed neural networks: A deep learning framework for solving forward and inverse problems involving nonlinear partial differential equations. *Journal of Computational Physics* **378**, 686–707 (2019)
- [136] Shah, A., Sabir, M., Bastian, P.: An efficient time-stepping scheme for numerical simulation of dendritic crystal growth. *European Journal of Computational Mechanics* **25**(6), 475–488 (2016)
- [137] Beneš, M., Chalupecký, V., Mikula, K.: Geometrical image segmentation by the allen-cahn equation. *Applied Numerical Mathematics* **51**(2-3), 187–205 (2004)
- [138] Shah, A., Sabir, M., Qasim, M., Bastian, P.: Efficient numerical scheme for solving the allen-cahn equation. *Numerical Methods for Partial Differential Equations* **34**(5), 1820–1833 (2018)
- [139] Shah, A., Yuan, L.: Numerical solution of a phase field model for incompressible two-phase flows based on artificial compressibility. *Computers & Fluids* **42**(1), 54–61 (2011)
- [140] Wu, J., Geng, X.: Inverse scattering transform and soliton classification of the coupled modified korteweg-de vries equation. *Communications in Nonlinear Science and Numerical Simulation* **53**, 83–93 (2017)
- [141] Khusnutdinova, K., Stepanyants, Y., Tranter, M.: Soliton solutions to the fifth-order korteweg–de vries equation and their applications to surface and internal water waves. *Physics of Fluids* **30**(2), 022104 (2018)